

1 MAX-DOAS observations of formaldehyde and nitrogen dioxide at three 2 sites in Asia and comparison with the global chemistry transport model 3 CHASER

4 Hossain Mohamed Syedul Hoque¹, Kengo Sudo^{1,2}, Hitoshi Irie³, Alessandro Damiani³, Manish Naja⁴, and Al
5 Mashroor Fatmi³

6 ¹Graduate School of Environmental Studies, Nagoya University, Nagoya, 4640064, Japan

7 ²Japan Agency for Marine-Earth Science and Technology (JAMSTEC), Kanagawa, 2370061, Japan

8 ³Center for Environmental Remote Sensing (CEReS), Chiba University, Chiba, 2638522, Japan

9 ⁴Aryabhatta Research Institute for Observational Sciences (ARIES), Manora Peak, Nainital-263001, Uttarakhand,
10 India

11

12 *Correspondence to:* Hossain Mohammed Syedul Hoque (hoque.hossain.mohammed.syedul.u6@f.mail.nagoya-
13 u.ac.jp or hoquesyedul@gmail.com)

14

15 **Abstract.** Formaldehyde (HCHO) and nitrogen dioxide (NO₂) concentrations and profiles were retrieved
16 from ground-based multi-axis differential optical absorption spectroscopy (MAX-DOAS) observations
17 during January 2017 - December 2018 at three sites in Asia: (1) Phimai (15.18°N, 102.5°E), Thailand;
18 (2) Pantnagar (29°N, 78.90°E) in the Indo Gangetic Plain (IGP), India; and (3) Chiba (35.62°N,
19 140.10°E), Japan. Retrievals were performed using the Japanese MAX-DOAS profile retrieval algorithm
20 ver. 2 (JM2). The observations were used to evaluate the NO₂ and HCHO partial columns and profiles (0
21 - 4 km) simulated using the global chemistry transport model (CTM) CHASER. The NO₂ and HCHO
22 concentrations at all three sites showed consistent seasonal variation throughout the investigated period.
23 Biomass burning affected the HCHO and NO₂ variations at Phimai during the dry season and at Pantnagar
24 during spring (March - May) and post-monsoon (September - November). Results found for the HCHO
25 to NO₂ ratio (R_{FN}), an indicator of high ozone sensitivity, indicate that the transition region (i.e., $1 < R_{FN}$
26 < 2) changes regionally, echoing the recent finding for R_{FN} effectiveness. Moreover, reasonable estimates
27 of transition regions can be derived, accounting for the NO₂ - HCHO chemical feedback.

28 The model was evaluated against global NO₂ and HCHO columns data retrieved from Ozone Monitoring
29 Instrument (OMI) observations before comparison with ground-based datasets. Despite underestimation,
30 the model well simulated the satellite-observed global spatial distribution of NO₂ and HCHO, with
31 respective spatial correlations (r) of 0.73 and 0.74. CHASER demonstrated good performance,
32 reproducing the MAX-DOAS retrieved HCHO and NO₂ abundances at Phimai, mainly above 500 m from
33 the surface. Model results agree with the measured variations within the one sigma standard deviation of
34 the observations. Simulations at higher resolution improved the modeled NO₂ estimates for Chiba,
35 reducing the mean bias error (MBE) for the 0 - 2 km height by 35%, but resolution-based improvements
36 were limited to surface layers. Sensitivity studies show that at Phimai, pyrogenic emissions contribute to
37 HCHO and NO₂ concentrations up to 50 and 35%, respectively.

38 1 Introduction

39 Formaldehyde (HCHO), the most abundant carbonyl compound in the atmosphere, is a high-yield product
40 of oxidization of all primary volatile organic compounds (VOCs) emitted from natural and anthropogenic
41 sources by hydroxyl radicals (OH). Oxidation of long-lived VOCs such as methane produces a global
42 HCHO background concentration of 0.2 – 1.0 ppbv in remote marine environments (Weller et al., 2000;
43 Burkert et al., 2001; Singh et al., 2004; Sinreich et al., 2005). Aside from oxidation of VOCs, the
44 significant sources of HCHO are direct emissions from biomass burning, industrial processes, fossil fuel
45 combustion (Lee et al., 1997; Hak et al., 2005; Fu et al., 2008), and vegetation (Seco et al., 2007).
46 However, oxidization of non-methane VOCs emitted from biogenic (e.g., isoprene) or anthropogenic (e.g.,
47 butene) sources govern the spatial variation of HCHO on a global scale (Franco et al., 2015). The sinks
48 of HCHO include photolysis at wavelengths shorter than 400 nm, oxidation by OH, and wet deposition,
49 thereby limiting the lifetime of HCHO to a few hours (Arlander et al., 1995).

50 Nitrogen dioxide (NO₂), an important atmospheric constituent, (1) participates in the catalytic
51 formation of tropospheric ozone (O₃), (2) acts as a catalyst for stratospheric ozone (O₃) destruction
52 (Crutzen, 1970), (3) contributes to the formation of aerosols (Jang and Kamens, 2001), (4) acts as a
53 precursor of acid rain (Seinfeld and Pandis, 1998), and (5) strongly affects radiative forcing (Solomon et
54 al. 1999; Lelieveld et al., 2002;). Nitrogen oxides (NO_x = NO (nitric oxide) + NO₂) are emitted from
55 natural and anthropogenic sources. Primary NO_x emission sources include biomass burning, fossil fuel

56 combustion, soil emissions, and lightning (Bond et al., 2001; Zhang et al., 2003). Not only do NO_x
57 emissions degrade air quality; they are leading air pollutant (Ma et al., 2013). Both HCHO and NO_2 are
58 important intermediates in the global VOC– HO_x (hydrogen oxides)– NO_x catalytic cycle, which governs
59 O_3 chemistry in the troposphere (Lee et al., 1997; Houweling et al., 1998; Hak et al., 2005; Kanakidou et
60 al., 2005). Thus, both trace gases play crucially important roles in tropospheric chemistry.

61 The observational sites examined for the present study have different atmospheric characteristics.
62 Thailand is strongly affected by pollution because of rapid economic development and urbanization.
63 Moreover, biomass burning in Southeast Asia is a significant source of O_3 precursors, contributing up to
64 30% of the total concentrations during the peak burning season (Amnuaylorajen et al., 2020; Khodmanee
65 et al. 2021). Because of rapid industrialization, India the second most populous country in the world, is
66 witnessing an increasing O_3 trend along with NO_2 and HCHO concentrations in all major cities (Mahajan
67 et al; 2015; Lu et al, 2018;). The Indo-Gangetic Plain (IGP), which covers ~21% of the Indian
68 subcontinent land area is hotspots of severe air pollution (Giles et al; 2005, Biswas et al; 2019). In contrast,
69 surface O_3 concentrations have shown an increasing trend in Japan, despite decreasing NO_x and VOC
70 concentrations related to emission control measures after 2000 (Irie et al., 2021). Therefore, observational
71 and modeling studies must be conducted to improve our quantitative understanding of the O_3 - NO_x -VOC
72 relation in these regions.

73 Multi-axis differential optical absorption spectroscopy (MAX-DOAS), a well-established, unique, and
74 powerful remote sensing method for measuring trace gases and aerosols, is based on the DOAS technique.
75 Aerosols and trace gases are quantified using selective narrowband (high frequency) absorption features
76 (Platt 1994; Platt and Stutz 2008). Spectral radiance measurements at different elevation angles (ELs) can
77 provide profile information about atmospheric trace gases and aerosols (Hönninger et al., 2004; Wagner
78 et al., 2004; Wittrock et al., 2004; Frieß et al., 2006; Irie et al., 2008a). Many studies have demonstrated
79 the retrieval of aerosol and trace gas concentrations and profiles from MAX-DOAS observations,
80 including NO_2 and HCHO (Clémer et al., 2010; Irie et al., 2011; Hendrick et al., 2014; Wang et al., 2014;
81 Franco et al., 2015; Frieß et al., 2016).

82 The ability of MAX-DOAS to provide information related to surface concentrations, vertical profiles,
83 and column densities makes it a good complement to ground-based in situ and satellite observations.

Moreover, the MAX-DOAS method uses narrowband absorption of the target compounds, thereby obviating any need for radiometric calibration of the instrument. Because of these advantages, MAX-DOAS systems are deployed for the assessment of aerosol and trace gases in regional and global observational networks such as BREDOM (Wittrock et al., 2004), BIRA-IASB (Cl  mer et al., 2010), and MADRAS (Kanaya et al., 2014). Such datasets are used, in but are not limited to, (1) air quality assessment and monitoring, (2) evaluation of chemistry-transport models (CTMS), and (3) validation of satellite data retrievals. Several studies have used MAX-DOAS datasets to validate tropospheric columns retrieved from satellite observations, including NO₂ and HCHO (Irie et al., 2008b; Ma et al., 2013; Chan et al., 2020; Ryan et al., 2020). However, limited MAX-DOAS datasets have been used to evaluate global CTMs. Vigouroux et al. (2009) and Franco et al. (2015) respectively used the MAX-DOAS HCHO datasets from Reunion Island and Jungfraujoch stations to evaluate the Intermediate Model of Annual and Global Evolution of Species (IMAGES) and GEOS-Chem model simulations. Kanaya et al. (2014) validated the Model for Interdisciplinary Research on Climate–Earth System Model – Chemistry (MIROC-ESM-CHEM) simulated NO₂ column densities with MAX-DOAS observations in Cape Hedo and Fukue in Japan. Kumar et al. (2021) used MAX-DOAS observations to evaluate the high-resolution regional model Meco(n)(MESSy-field ECHAM and COSMO model nested n times).

For this study, NO₂ and HCHO profiles retrieved from MAX-DOAS observations from the International air quality and sky research remote sensing (A-SKY) (<http://atmos3.cr.chiba-u.jp/a-sky/>) network sites are used to evaluate the global Chemical Atmospheric General Circulation Model for the Study of Atmospheric Environment and Radiative Forcing (CHASER; Sudo et al., 2002). The three A-SKY sites of - (1) Phimai in Thailand (15.18  N, 102.56  E), (2) Pantnagar (29  N, 78.90  E) in the IGP in India, and (3) Chiba (35.62  N, 140.10  E) in Japan, are respectively representative of rural, semi-rural, and urban environments. CHASER has been used mostly for global-scale research (Sudo et al., 2007; Sekiya et al., 2014, 2018; Miyazaki et al., 2017). The study described herein is the first reported attempt to evaluate the CHASER-simulated NO₂ and HCHO profiles using MAX-DOAS observations in three different atmospheric environments. Moreover, few reports of the literature have described the use of MAX-DOAS datasets to evaluate global CTMs in South Asia and South-east Asia. Overall, this study was conducted

111 to provide important insights into model performances and to help reduce model uncertainties related to
112 NO₂ and HCHO simulations in these regions.

113 The paper is structured in the following manner. First, the observation sites, MAX-DOAS
114 instrumentation, and retrieval strategies are described in section 2. Section 2 also includes a short
115 description of the CHASER model and Ozone Monitoring Instrument (OMI) HCHO and NO₂ retrievals.
116 Next, the observations and the evaluation results are described in sections 3. Finally, the sensitivity study
117 results are provided in section 3.4. and the concluding remarks in section 4.

118

119

120 **2 Observations, datasets, and methods**

121

122 **2.1 Site Information**

123 Continuous MAX-DOAS observations at Chiba, Phimai, and Pantnagar started respectively in 2012,
124 2014, and 2017. The measurements from January 2017 to December 2018 at all three sites are discussed
125 herein. Phimai, a rural site, is located ~260 km north-east of the Bangkok metropolitan area and is unlikely
126 to be affected by vehicular and industrial emissions. However, the site is affected by biomass burning
127 during January - April. Two major air streams: the dry, cool north-east monsoon during November – mid-
128 February and the wet, warm south-west monsoon during mid-May – September affect the climate in
129 Phimai. As described by, Hoque et al. (2018), the climate classifications of Phimai are the (a) dry season
130 (January – April), and (b) wet season (June – September).

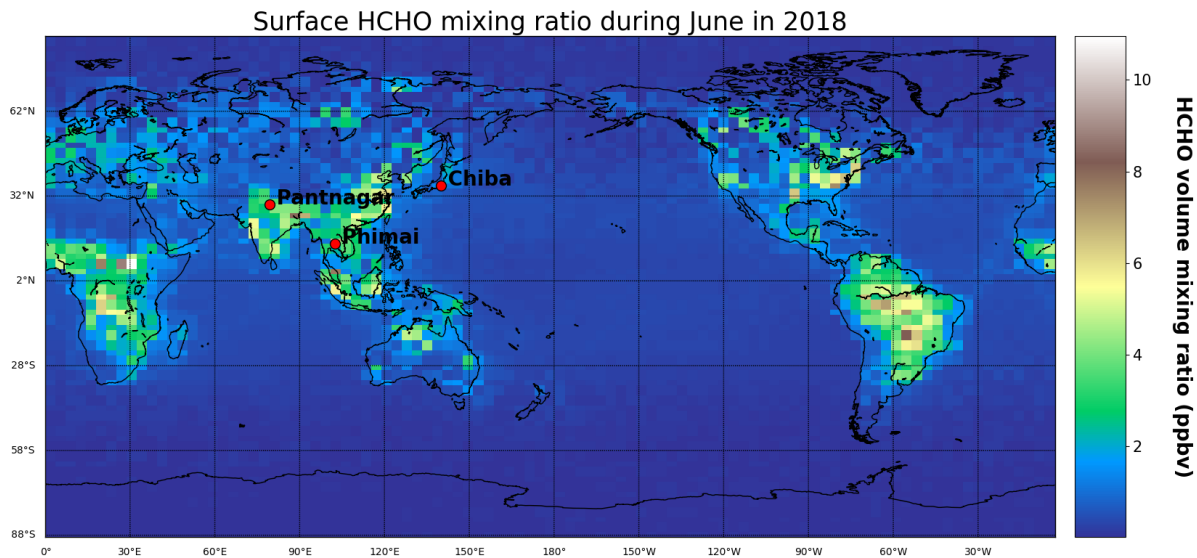
131 Pantnagar, a semi-urban site in India, is located in the IGP. The Indian capital of New Delhi is situated
132 at ~225 km south-west of the site. The low-altitude plains are on the south and west sides of the site. The
133 Himalayan mountains are located to the north and east. An important roadway with moderate traffic
134 volume and a small local airport lies within 3 km of the site. Rudrapur (~12 km south-west of Pantnagar)
135 and Haldwani (~ 25 km north-east of Pantnagar) are the two major cities near Pantnagar, where non-
136 combustible industries are located (Joshi et al., 2016). The climate classification at Pantnagar is the

137 following: (1) winter (December–February), (2) spring (March–May), (3) summer monsoon (June–
138 August), and (4) autumn (September–November).

139 Chiba, an urban site, is located ~40 km south-east of the Tokyo metropolitan region. Tokyo Bay,
140 large-scale industries, and residential areas are located within a 50 km radius. Chiba has four distinct
141 seasons: (1) spring (March–May), (2) summer (June–August), (3) autumn (September–November), and
142 winter (December– February). The locations of the three sites are depicted in Fig. 1.

143

144



145 **Figure 1:** Surface HCHO mixing ratio in June 2018, simulated using the CHASER model. The red points
146 represent the locations of the observation sites, which are part of the A-SKY network.

147

148

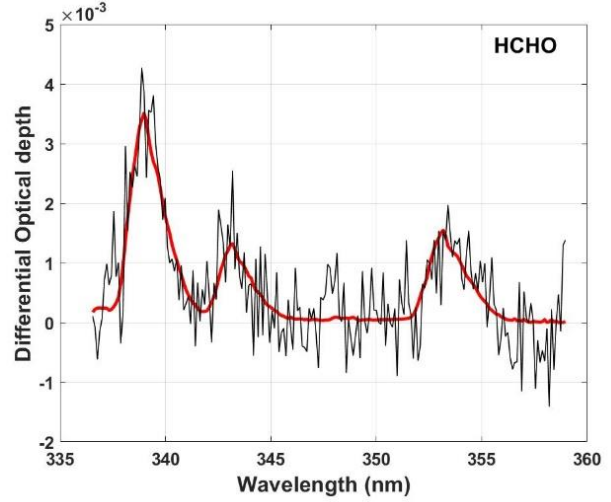
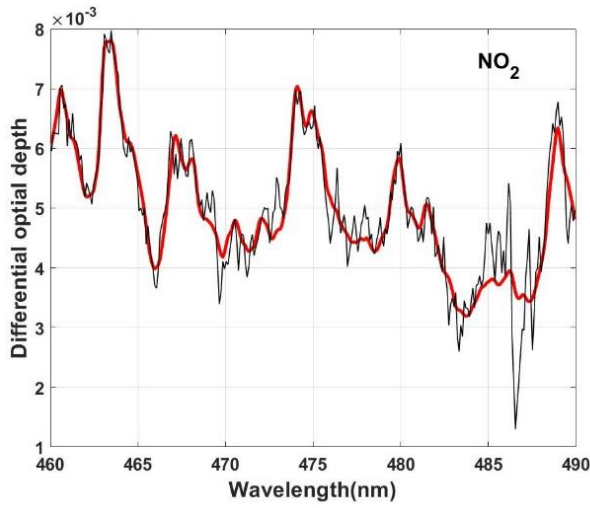
149 2.2 MAX-DOAS retrieval

150 The MAX-DOAS systems used for continuous observations at the three sites participated in the Cabauw
151 Intercomparison Campaign of Nitrogen Dioxide measuring Instruments (CINDI) (Roscoe et al., 2010)
152 and CINDI-2 (Kreher et al., 2020) campaigns. The instrumentation setup is described by Irie et al. (2008,
153 2011, 2015). The indoor part of the MAX-DOAS systems consists of an ultraviolet-visible (UV-VIS)
154 spectrometer (Maya2000Pro; Ocean Optics Inc.) embedded in a temperature-controlled box. The outdoor
155 unit consists of a single telescope and a 45° inclined movable mirror on a rotary actuator, used to perform
156 reference and off-axis measurements. The high-resolution spectra from 310–515 nm is recorded at six
157 elevation angles (ELs) of 2°, 3°, 4°, 6°, 8°, and 70° at the Chiba and Phimai sites. At the Pantnagar site,
158 measurements are conducted at ELs of 3°, 4°, 5°, 6°, 8°, and 70°. The sequences of the ELs at all the sites
159 were repeated every 15 min. The reference spectra are recorded at EL of 70° instead of 90° to avoid
160 saturation of intensity. Because all the ELs were considered in the box air mass factor (A_{box}) calculation
161 to retrieve the vertical profile, the choice of reference EL (70° or 90°) is not an important issue for this
162 study. The off-axis ELs are limited to $< 10^\circ$ to reduce the systematic error in the in-oxygen collision
163 complex (O_4) fitting results (Irie et al., 2015), thereby maintaining high sensitivity in the lowest layer of
164 the retrieved aerosol and trace gas profiles. Daily wavelength calibration using the high-resolution solar
165 spectrum from Kurucz et al. (1984) is performed to account for the spectrometer's long-term degradation.
166 The spectral resolution (full width half maximum: FWHM) is about 0.4 nm at 357 and 476 nm. The
167 concentrations and profiles of aerosol and trace gases are retrieved using the Japanese vertical profile
168 retrieval algorithm (JM2 ver. 2) (Irie et al., 2011, 2015). The algorithm works in three steps: (1) DOAS
169 fittings, (2) profile/column retrieval of aerosol, and (3) profile/column retrieval of trace gases. Irie et al.
170 (2008a, 2008b, 2011, 2015) described the retrieval procedures, and the error estimates. Herein we provide
171 a short overview.

172 First, the differential slant column density ($\Delta SC D$) of trace gases is retrieved using the DOAS
173 technique (Platt 1994), which uses the nonlinear least-squares spectral fitting method, according to the
174 following equation :

$$\ln I(\lambda) = \ln(I_o(\lambda) - c(\lambda)) - \sum_i^n \sigma_i(\lambda) \Delta SCD_i - p(\lambda) \quad (1)$$

Therein, $I_o(\lambda)$ represents the reference spectrum measured at time t . $I_o(\lambda)$ is derived by interpolating two reference spectra (i.e., EL=70°) within 15 min before and after the complete sequential scan of the off-axis ELs at time t . ΔSCD represents the difference between the slant column density along the off-axis and reference spectrum. Second- and third-order polynomials are fitted to account, respectively, the wavelength-dependent offset $c(\lambda)$ and the effect of molecular and particle scattering $p(\lambda)$. In addition, $c(\lambda)$ accounts for the influence of stray light. The HCHO ΔSCD and NO₂ ΔSCD are retrieved respectively, from the fitting windows of 340–370 and 460–490 nm. Significant O₄ absorptions in the 338–370 and 460–490 nm fitting windows are used to retrieve the O₄ ΔSCD s. The absorption cross-section data sources and the fitted absorbers in the HCHO and NO₂ fitting windows are given in Table 1. Figure 2 presents an example of the fitting results. O₄ fittings in both retrieval windows are shown in Fig S1 (supplementary information).



188 **Figure 2:** Examples of spectral fitting of NO₂ and HCHO, where red and black lines respectively show the scaled
 189 cross-section and the summation of scaled cross-sections and fitting residuals. The example shows the
 190 measurements of 10 April 2017, in Phimai at 10:00 LT at an EL of 2°.

191 In the second step, the aerosol optical depth (AOD) τ and the vertical profiles of the aerosol extinction
 192 coefficient (AEC) k are retrieved using the approach developed by Irie et al, (2008a) which is based on
 193 the optimal estimation method (Rogers, 2000). In this approach, the measurement vector y (representing
 194 the quantities to be fitted) and state vector (representing the retrieved quantities) is defined as

195

$$196 \quad y = (O_4 \Delta SCD(\Omega_1) \dots \dots \Delta SCD(\Omega_n))^T \quad (2) \text{ and}$$

$$197 \quad x = (\tau F_1 F_2 F_3)^T \quad (3),$$

198

200 **Table 1.** Cross-section data references and absorbers fitted in the HCHO and NO₂ windows

| Cross-section | Absorbers fitted | Data Source |
|------------------|--|--------------------------------------|
| O ₃ | | Bougmil et al. (2003), 223K |
| NO ₂ | O ₃ , NO ₂ , H ₂ O, O ₄ , Ring | Vandaele et al. (1996), 295K |
| BrO | | Fleischmann et al. (2004), 223K |
| Ring | | Chance and Spurr (1997) |
| H ₂ O | | Vandaele et al. (2005), 280K |
| O ₄ | | Hermans et al. (2003), 296K |
| HCHO | O ₃ , NO ₂ , HCHO, BrO, O ₄ , Ring | Meller and Moortgart (2000), 293k |

201

202

203 where n stands for the number of measurements within one complete scan of an EL sequence. Also, Ω
204 denotes the viewing geometry and includes three components: solar zenith angle (SZA), EL, and relative
205 azimuth angle (RAA). The F values determine the profile shape, with values between 0 and 1. The partial
206 AOD for 0–1, 1–2, 2–3, and above 3 km layers were defined respectively as $AOD \cdot F_1$, $AOD \cdot (1-F_1) F_2$,
207 and $AOD \cdot (1-F_1) (1-F_2) F_3$, and $AOD \cdot (1-F_1) (1-F_2) (1-F_3)$. The AEC profile from 3 to 100 km is derived

208 assuming a fixed value at 100 km and exponential AEC profile shape with a scaling height of ~1.6 km.
 209 The k value at 100 km was estimated from Stratospheric Aerosol and Gas Experiment III (SAGE III)
 210 aerosol data ($\lambda=448$ and 521 nm) taken at altitudes of 15–40 km. The negligible influence of such
 211 assumptions on the retrievals in the lower troposphere has been demonstrated in sensitivity studies
 212 reported by Irie et al (2012). Similarly, the AEC profiles at 2–3, 1–2, and 0–1 km were derived. Such
 213 parameterization provides the advantage that the AEC profile can be retrieved using only the apriori
 214 knowledge of the F values (profile shape) and little or no information related to the absolute AEC values
 215 in the troposphere. Irie et al. (2008a) demonstrated that the relative variability of the profile shape, in
 216 terms of 1-km averages, is smaller than that of the absolute AEC values. AEC profile shapes
 217 corresponding to different F values is shown in Fig.S2 (supplementary information). However, the
 218 vertical resolution and the measurement sensitivity cannot be derived directly with such a
 219 parameterization (Irie et al., 2008a; 2009). The retrievals and simulations conducted by other groups for
 220 similar geometries (i.e., Frieß et al., 2006) are used to overcome such limitations. The apriori values used
 221 for this study were similar to those reported by Irie et al. (2011): $AOD = 0.21 \pm 3.0$, $F_1 = 0.60 \pm 0.05$, F_2
 222 $= 0.80 \pm 0.03$, and $F_3 = 0.80 \pm 0.03$.

223 Then, a lookup table (LUT) of the box air mass factor (A_{box}) vertical profile at 357 and 476 nm is
 224 constructed using the radiative transfer model JACOSPAR (Irie et al., 2015), which is based on the Monte
 225 Carlo Atmospheric Radiative Transfer Simulator (MCARaTS) (Iwabuchi, 2006). The values of the single-
 226 scattering albedo (s), asymmetry parameter (g), and surface albedo were, respectively, 0.95, 0.65 (under
 227 the Henyey-Greenstein approximation), and 0.10. The U.S. standard atmosphere temperature and pressure
 228 profiles were used for radiative transfer calculations. Uncertainty of less than 8% related to the usage of
 229 fixed values of s , g , and a were estimated from sensitivity studies (i.e., Irie et al 2012). Results obtained
 230 from JACOSPAR are validated in the study reported by Wagner et al. (2007). The optimal aerosol load
 231 and the A_{box} profiles are derived using the A_{box} LUT and the O_4 Δ SCD at all ELs.

232 In the third step, the A_{box} profiles, HCHO and NO_2 Δ SCDs, and the nonlinear iterative inversion
 233 method are used to retrieve the HCHO and NO_2 vertical column densities (VCDs) and profiles. Here the
 234 NO_2 retrieval is explained.

235

For trace gas retrieval, the measurement vector and state vector are defined as

$$y = (NO_2\Delta SCD(\Omega_1) \dots \dots NO_2\Delta SCD(\Omega_n))^T \quad (4) \text{ and}$$

$$x = (VCD f_1 f_2 f_3)^T \quad (5)$$

VCD represents the vertical column density below 5 km. The f values are the profile shape factors. Above the 5 km layer, fixed profiles are assumed. Similarly, to aerosol retrieval, the partial VCD values for the 0–1, 1–2, 2–3, and 3–5 km is defined respectively as $VCD \cdot f_1$, $VCD \cdot (1-f_1) f_2$, $VCD \cdot (1-f_1) (1-f_2) f_3$, and $VCD \cdot (1-f_1) (1-f_2) (1-f_3)$. Finally, the volume mixing ratio (VMR) is calculated using the partial VCD, and U.S. standard atmosphere temperature and pressure data scaled to the respective surface measurements.

The calculated vertical profile is converted to $NO_2 \Delta SCDs$ using the A_{box} LUT constructed for aerosol retrieval. However, the trace gas wavelengths differed from the representative wavelengths of A_{box} LUT (357 and 476 nm). Therefore, the AOD at the trace gas wavelength is estimated, converting the retrieved AOD to the closer aerosol wavelength of 357 or 476 nm, assuming the Angstrom exponent value of 1.00. The choice of the Angstrom exponent value can induce uncertainty in the retrieved VCDs. However, such uncertainty was found to be non-significant compared to that of A_{box} profiles. Uncertainty in the A_{box} profiles are assumed to be as high as 30 to 50%. Such values are derived empirically from comparison with sky radiometer and LIDAR observations (i.e., Irie et al., 2008b). Then, the A_{box} profiles from the LUT corresponding to the recalculated AOD values are selected. The dependence of the A_{box} profiles on the concentration profiles is expected to be low because both HCHO and NO_2 are optically thin absorbers (Wagner et al., 2007; Irie et al., 2011). For every 15 min (time necessary for one complete scan of ELs), 20% (the mean ratio of the retrieved VCD to maximum ΔSCD) of the maximum trace gas $\Delta SCDs$ is used as a priori information for the VCD retrievals. The a priori error is set to 100% of the maximum trace gas ΔSCD . Figure 3 presents the mean averaging kernel (AK) of the HCHO and NO_2 retrievals during the dry season at Phimai. The area (Rodgers, 2000) provides an estimate of the measurement contribution to the retrieval. The total area is the sum of all the elements in the AK and weighted by the a priori error (Irie et al. 2008a). The areas for VCD and f_1 of NO_2 retrieval are 1 and 0.6, respectively. The f_2 and f_3 values are much smaller. Consequently, at first, the a priori profiles were scaled, and later f values determined

the profile shape. The VCD area is close to unity, and therefore, the retrieved VCD is independent of the a priori values. Irie et al (2008) conducted sensitivity studies of choice of the f values and reported negligible effect on the retrievals.

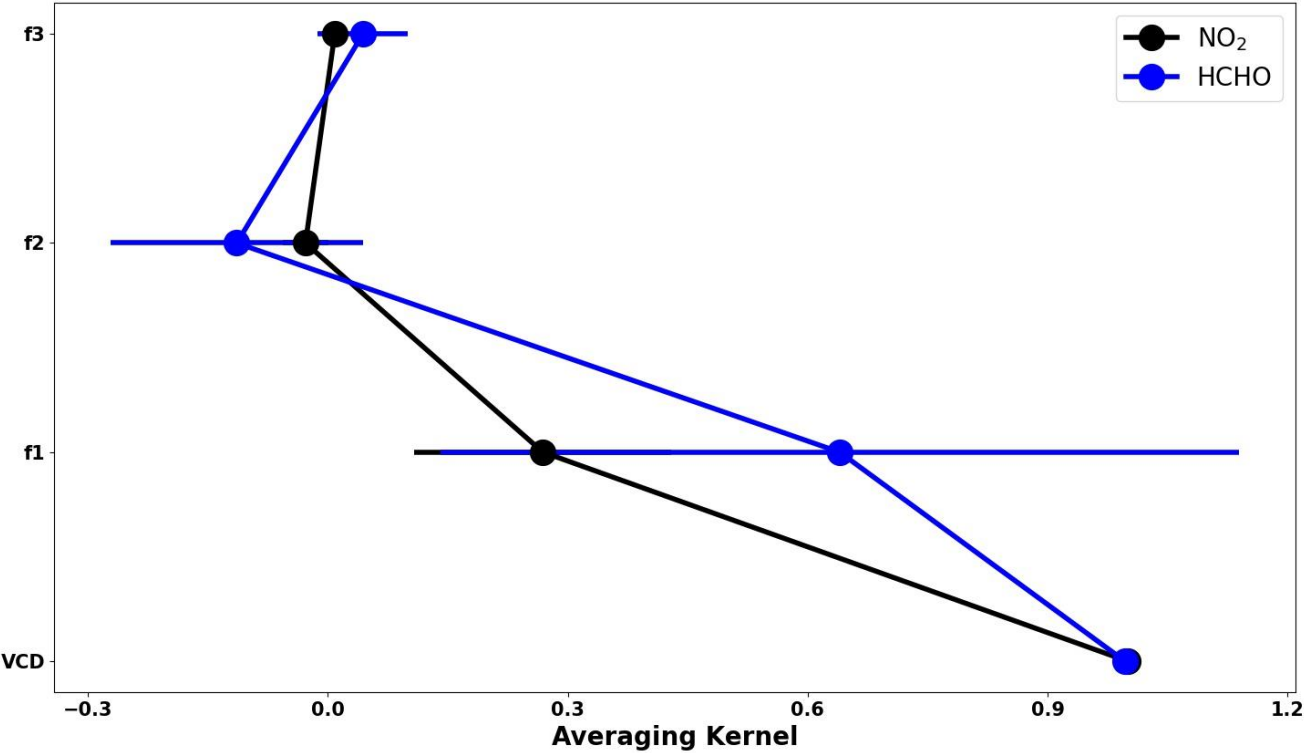


Figure 3: Mean averaging kernel of the NO₂ and HCHO retrievals from observations at Phimai during 2017. The error bars represent the 1-sigma standard deviation of the mean values.

The total error of the retrieval consists of random and systematic errors. The measurement error covariance matrix constructed from the residuals of the respective trace gas Δ SCDs is used to estimate the random error. The systematic error is calculated while assuming uncertainties as high as 30 and 50% in the retrieved AOD (or the corresponding A_{box} values). Table 2 shows the total estimated error. Aside from the random and systematic error, more sources of error might exist. For instance, the bias in the ELs

277 can induce uncertainties in the retrieved products. However, Hoque et al. (2018) demonstrated that such
278 biases had a non-significant effect on the final retrieved products, mostly less than 5%.

279 The cloud screening procedure is similar to that described by Irie et al. (2011) and by Hoque et al.
280 (2018a, 2018b). During the retrieval steps, retrieved AOD values greater than 3 are excluded, because
281 optically thick clouds are primarily responsible for such large optical depth. Filtering based on the
282 residuals of O₄ and the trace gas ΔSCDs is also used to screen clouds. Larger residuals likely occur due
283 to two reasons: (1) when the constructed profile is too simple to represent the true profile, particularly
284 with a steep vertical gradient of extinction due to clouds, and (2) rapid changes in optical depth within 30
285 min (time for one complete scan) (Irie et al, 2011). The screening criteria are: respective residuals of O₄,
286 HCHO, and NO₂ ΔSCDs < 10%, < 50%, and <20%, and the degrees of freedom of retrievals greater than
287 1.02. The threshold values were determined statistically corresponding to the mode plus one sigma (1σ)
288 in the logarithmic histogram of relative residuals.

289
290 **Table 2.** Estimated Errors (%) for the NO₂ and HCHO concentration in 0-1 km layer, retrieved using the
291 JM2 algorithm

| Retrieved Product | Random error | Systematic error | Error related to instrumentation | Total error |
|----------------------|--------------|------------------|-------------------------------------|-------------|
| NO ₂ | 10 | 12 | 5 | 16 |
| HCHO | 16 | 25 | 5 | 30 |

292
293
294 **2.3 CHASER simulations**

295 CHASER 4.0 (Version 4) (Sudo et al., 2002; Sudo and Akimoto, 2007; Sekiya and Sudo, 2014), coupled
296 online with the MIROC-AGCM atmospheric general circulation model (AGCM) (K-1 model developers,
297 2004) and the SPRINTARS aerosol transport model (Takemura et al., 2005, 2009), is a global chemistry
298 transport model used to study the atmospheric environment and radiative forcing. In addition, several

299 updates, including the introduction of aerosol species (sulfate, nitrate, etc.) and related chemistry,
 300 radiation, and cloud processes, have been implemented in the latest version of CHASER.
 301 CHASER can calculate the concentrations of 92 species through 263 chemical reactions (gaseous,
 302 aqueous, and heterogeneous chemical reactions) considering the chemical cycle of O_3 – HO_x – NO_x – CH_4 –
 303 CO along with oxidation of non-methane volatile organic compounds (NMVOCs)(Miyazaki et al., 2017).
 304 The chemical mechanism is largely based on the master chemical mechanism (MCM,
 305 <http://mcm.york.ac.uk>)(Jenkin et al., 2015). CHASER simulates the stratospheric O_3 chemistry
 306 considering the Chapman mechanisms, catalytic reactions related to halogen oxides (HO_x , NO_x , ClO_x ,
 307 and BrO_x), and polar stratospheric clouds (PSCs). Resistance-based parameterization (Wesely, 1989),
 308 cumulus convection, and large-scale condensation parameterizations are used to calculate dry and wet
 309 depositions. The piecewise parabolic method (Colella and Woodward, 1984)

310

311 **Table 3:** Settings of the CHASER simulations used in this study

| Simulation | Anthropogenic emissions | Pyrogenic emissions | Biogenic emissions | Soil NO _x emission | Other physical and chemical processes |
|--------------------|-------------------------|-------------------------|--------------------|-------------------------------|---------------------------------------|
| Standard | ON | ON | ON | ON | ON |
| L1_HCHO | ON | Pyrogenic VOCs switched | ON | ON | ON |
| L1_opt | ON | OFF | Reduced by 50% | ON | ON |
| L1_NO ₂ | ON | ON | ON | OFF | ON |

| | | | | | |
|-----------|---------------|----|----|----|----|
| L2 | Anthropogenic | ON | ON | ON | ON |
| | VOC emissions | | | | |
| | switched OFF | | | | |

312

313 and the flux-form semi-Lagrangian schemes (Lin and Rood, 1996) calculate advective tracer transport.
 314 CHASER simulates tracer transport on a sub-grid scale in the framework of the prognostic Arakawa–
 315 Schubert cumulus convection scheme (Emori et al., 2001) and the vertical diffusion scheme (Mellor and
 316 Yamada, 1974). In this study, CHASER simulations were conducted at a horizontal resolution of $2.8^\circ \times$
 317 2.8° , with 36 vertical layers from the surface to ~50 km altitude and a typical time step of 20 min. The
 318 meteorological fields simulated by MIROC-AGCM were nudged toward the six-hourly NCEP FNL
 319 reanalysis data at every model time step.

320 The anthropogenic, biomass burning, lightning, and soil emissions of NO_x were incorporated into
 321 CHASER simulations. Anthropogenic emissions were based on HTAP_v2.2 for 2008. Biomass burning
 322 and soil emissions from the ECMWF/MAC (Global Fire Assimilation System (GFAS)) reanalysis were
 323 used. The biogenic emissions for VOCs are based on the process-based biogeochemical model the
 324 Vegetation Integrative Simulator for Trace gases (VISIT) (Ito and Inatomi, 2012) simulations. The NO_x
 325 production from lightning is calculated based on the parameterization of Price and Rind (1992) linked to
 326 the convection scheme of the AGCM (Sudo et al., 2002). Isoprene, terpene, acetone, and ONMV
 327 emissions estimates in the VISIT inventory during July were 2.14×10^{-11} , 4.43×10^{-12} , 1.60×10^{-12} , and
 328 $9.93 \times 10^{-13} \text{ kgCm}^{-2}\text{s}^{-1}$. Global NO_x emissions of 43.80 TgNyr^{-1} are used in the simulations, considering
 329 industries (23.10 TgNyr^{-1}), biomass burning (9.65 TgNyr^{-1}), soil (5.50 TgNyr^{-1}), lightning (5 TgNyr^{-1}),
 330 and aircrafts (0.55 TgNyr^{-1}) as significant sources. Global isoprene emissions from vegetation were set to
 331 400 TgCyr^{-1} .

NO_x emissions in India were estimated as 14 Tg/yr in 2016, almost two-fold increase since 2005 (~8 Tg/yr), with the energy and transportation sector being the largest contributor (Sadavarte et al 2014). Indian anthropogenic non-methane VOCs (NMVOCs) emissions in 2010 were estimated ~ 10 Tg/yr, with respective contributions of 60, 16, and 12% from residential, solvents, and the transport sector (Sharma et al 2015). In Japan, vehicular exhausts (14 - 25%), gasoline vapor (9 - 16%), liquefied natural gas (7 - 10%), and liquefied petroleum gas (49 - 71%) contribute to the total VOC concentrations (Morino et al., 2011), with annual NMVOC emission of ~2 Tg (Kannari et al., 2007). Annual NO_x emissions in Japan and Thailand in 2000 was estimated as ~2000 and 591 kt/yr, with the largest contribution from transport-oil use, followed by the energy and industrial sector (Ohara et al., 2007). Annual anthropogenic VOC emissions in Thailand are approximately 0.9 Tg, with 43, 38, and 20% contributed, respectively, from industrial, residential and transportation sectors (Woo et al; 2020). Multiple CHASER simulations with different settings used for sensitivity studies are presented in Table 3.

345

2.4 Satellite observations

Tropospheric NO₂ and HCHO retrievals from the Ozone monitoring Instrument (OMI) were also used to evaluate the model simulations. The ultra-violet nadir-viewing spectrometer OMI, on board the Aura satellite measures backscattering solar radiation covering the spectral range of 270 – 500 nm (Levelt et al., 2006). In an ascending sun-synchronous polar-orbit, OMI crosses the equator at 13:40 LT (local time) (Zara et al., 2018). OMI measures at a spatial resolution of 13 × 24 km² and provides daily global coverage of various trace gases including NO₂ and HCHO. The NO₂ and HCHO datasets were obtained respectively from the TEMIS (www.temis.nl, last accessed on 2022/04/23) and aeronomie (<https://h2co.aeronomie.be/>, last accessed 2022/05/03) websites. NO₂ tropospheric columns retrieved using the DOMINO version 2.0 (Boersma et al., 2011) algorithm were used for the analysis. Data meeting the following criteria were selected: cloud fraction < 0.5, SZA < 70°, surface albedo < 0.3, quality flags = 0, and cross-track quality flags = 0. For HCHO, we used the BIRA-IASB v14 (De Smedt et al 2015)

358 retrieved products. The data filtering criteria was the following: cloud fraction < 0.4, SZA<70°, AMF >
359 0.2, quality flag=0, and cross-track quality flag =0.

360

361

362 **3 Results and discussion**

363 **3.1 Results from MAX-DOAS observations**

364 **3.1.1 HCHO seasonal variation**

365 The monthly mean HCHO mixing ratios in the 0–1 and 0–2 km layers from January 2017 – December
366 2018 and the corresponding one sigma (1σ) standard deviations **indicating** the variation ranges for the
367 three sites are presented in Fig. 4. The HCHO levels at the Phimai site show a consistent seasonal cycle,
368 characterized by high VMRs during the dry season. Such enhancement is related to the influence of
369 biomass burning during the dry season, which has been well documented in the work of Hoque et al.
370 (2018). The HCHO mixing ratio at Phimai reach a peak in March or April, with a maximum of 4 – 6
371 ppbv. The variation in the peak concentration and timing depends mainly on the intensity of biomass
372 burning activities. During the wet season, the HCHO concentrations are mostly within 2–3 ppbv,
373 indicating a two-fold increase in HCHO abundances during the dry season. The daily mean HCHO
374 amounts (0 –1 km) are 0.78 - 9.84 ppbv, representing seasonal modulation of 134%.

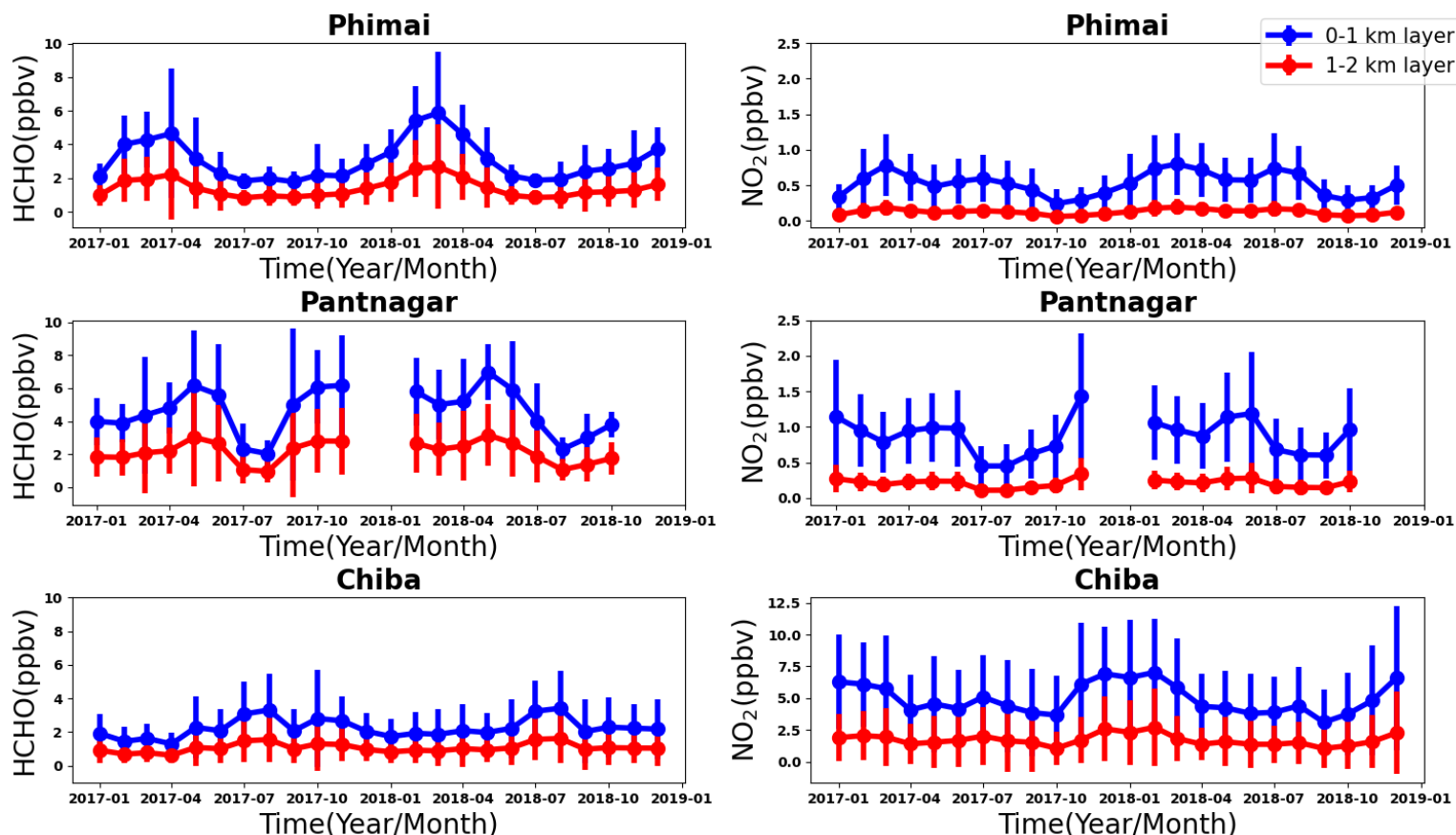


Figure 4: Seasonal variations in the HCHO (left panel) and NO₂ (right panel) mixing ratios in the 0 - 1 (blue) and 1 - 2 (red) km layers at Phimai, Pantnagar, and Chiba. The error bars represent the one sigma standard deviation of the mean values. The gaps in the plots for the Pantnagar site indicate the unavailability of observations during the investigated period.

380

381

Seasonal variation of HCHO in the 0–1 km layer at the Pantnagar site has been elucidated by Hoque et al. (2018b). Here, the results are replotted to verify the consistency of the seasonal variations. Observations made during autumn 2018 were not available because of problem with the spectrometer. Consistent seasonal variation of HCHO abundances is observed at the Pantnagar site, with enhanced concentrations during the spring. The Pantnagar site is affected by biomass burning during spring and autumn (Hoque et al., 2018b), explaining the high mixing ratios found during spring. In both years, the

388 maximum HCHO mixing ratios are ~ 6 ppbv. The springtime peak occurred in May. The HCHO
389 concentrations during the monsoon are $\sim 35\%$ lower than in the spring, indicating a strong effect of the
390 monsoon on the HCHO concentrations found for Pantnagar. The seasonal modulation of HCHO at
391 Pantnagar estimated from the daily mean concentrations is 107%. The peak HCHO mixing ratio at
392 Pantnagar is almost twice that of in Pune city (~ 3 ppbv) (Biswas and Mahajan, 2021), a site in the IGP
393 region. The HCHO seasonality at the two sites are found to be dissimilar, because of differences in the
394 VOC sources, however, lower mixing ratios during the monsoon is consistent. From another site in the
395 IGP region (i.e., Mohali), Kumar et al., (2020) reported lowest HCHO VCDs during March 2014 and
396 2015, attributing them to lower biogenic and anthropogenic VOC emissions. At Pantnagar, the lowest
397 HCHO mixing ratios are observed during the monsoon. The rainfall events in the IGP region shows strong
398 annual variability (Fukushima et al. 2019). Discrepancies between the sites might be related to the rainfall
399 pattern.

400 Under the influence of biomass burning, the maximum monthly HCHO mixing ratios at Phimai and
401 Pantnagar are similar (~ 6 ppb). The maximum instantaneous HCHO VMR during biomass burning
402 influence in Phimai and Pantnagar are, respectively, 26 and 30 ppbv. Zarzana et al. (2017) reported HCHO
403 abundances of ~ 60 ppbv in fresh biomass plumes in the US. The lower values obtained from our
404 measurements might be attributable to (1) more aged plumes intercepted by the MAX-DOAS instruments
405 and (2) differences in the types of biomass fuel used. Comparison to reports of literature indicates that the
406 retrieval of HCHO under biomass burning is reasonable.

407 The summertime maximum and wintertime minimum characterize the seasonal variations of HCHO at
408 the Chiba site, with a peak at ~ 3 ppbv. The HCHO concentrations are ~ 2 ppbv during other seasons,
409 which are similar to the HCHO concentrations in Phimai during the wet season. The seasonal variation
410 amplitudes of HCHO at Chiba is $\sim 94\%$. For a site with similar seasonal variation (i.e., summertime
411 maximum and wintertime minimum), Franco et al. (2015) reported HCHO seasonal modulation of 88%.

412 The HCHO VMRs in the 1–2 km layers at all three sites are lower, almost 50% the value of the
413 concentrations in the 0–1 km layer. The HCHO seasonal variation amplitudes at Phimai, Pantnagar, and
414 Chiba sites are, respectively, 131%, 102%, and 90% when calculated based on the HCHO concentration
415 in the 1–2 km layers. The modulation was even lower when retrieved values for the 2–3 km layer is used.

3.1.2 NO₂ seasonal variation at the three sites

Figure 4 also shows the seasonal variation of NO₂ in the 0–1 and 1–2 km layers at the three sites. The error bars represent the 1 σ standard deviation of the mean values. The NO₂ seasonal variations at Phimai and Pantnagar sites are similar to those of HCHO. Pronounced peaks attributable to biomass burning influence is observed during the dry season at Phimai (~0.8 ppbv) and during spring (1.2 ppbv), and post-monsoon (1.4 ppbv) at Pantnagar. The lowest NO₂ mixing ratios at Phimai and Pantnagar are, respectively, ~0.2 and 0.5 ppbv. The NO₂ VMRs at Chiba is higher (~7 ppbv) during winter. The longer lifetime of NO_x and lower NO/NO₂ ratio because of lower photochemical activity in winter lead to high NO₂ mixing ratios at Chiba (Irie et al., 2021).

At Phimai, the NO₂ mixing ratios in both seasons are similar. However, when Hoque et al. (2018a) reported the seasonal variations in NO₂ at Phimai during 2015 – 2018, the dry season mixing ratios were higher. Table 4 shows the number of fire events during the dry seasons during 2015 - 2018. The fire data are extracted from the MODIS Active Fire Detections database (<https://firms.modaps.eosdis.nasa.gov>, last accessed on 2021/12/15). Data fulfilling the following criteria were chosen – (a) data points located within 100 km of the Phimai site, (b) confidence of the data greater than 70%, and (c) observations during the daytime. The lower fire counts during 2017 - 2018 compared to those of 2015 - 2016 period coincide with the lower NO₂ levels in the former. Fire counts varied between 2017 and 2018 but did not affect the NO₂ levels. However, HCHO levels changed with the number of fire occurrences between 2015 – 2018 (i.e., Figure 4 and Hoque et al., 2018a).

At such low NO₂ levels at Phimai, soil NO_x emissions are likely to make a greater contribution to NO₂. Although NO₂ is not emitted directly from soils, biological processes emit NO, which is rapidly converted to NO₂ (Hall et al., 1996). In addition, many studies have established a relation between soil moisture and NO emissions (Carden et al., 1993; Zheng et al., 2000; Schindlbacher et al., 2004; Huber et al., 2020). The potential contribution of soil NO_x emissions, as inferred from CHASER simulations, is discussed in section 3.4.2.

Table 4: Number of fire events occurring during the dry season (January - April) at Phimai from 2015 - 2018. Selection criteria of the data are the following: (1) situated within 100 km of the site, (2) confidence level > 70%, and (c) daytime measurements.

| Dry season years | Number of fire events |
|------------------|-----------------------|
| 2015 | 84 |
| 2016 | 98 |
| 2017 | 62 |
| 2018 | 77 |

3.1.3.1 The HCHO to NO₂ ratio (R_{FN}):

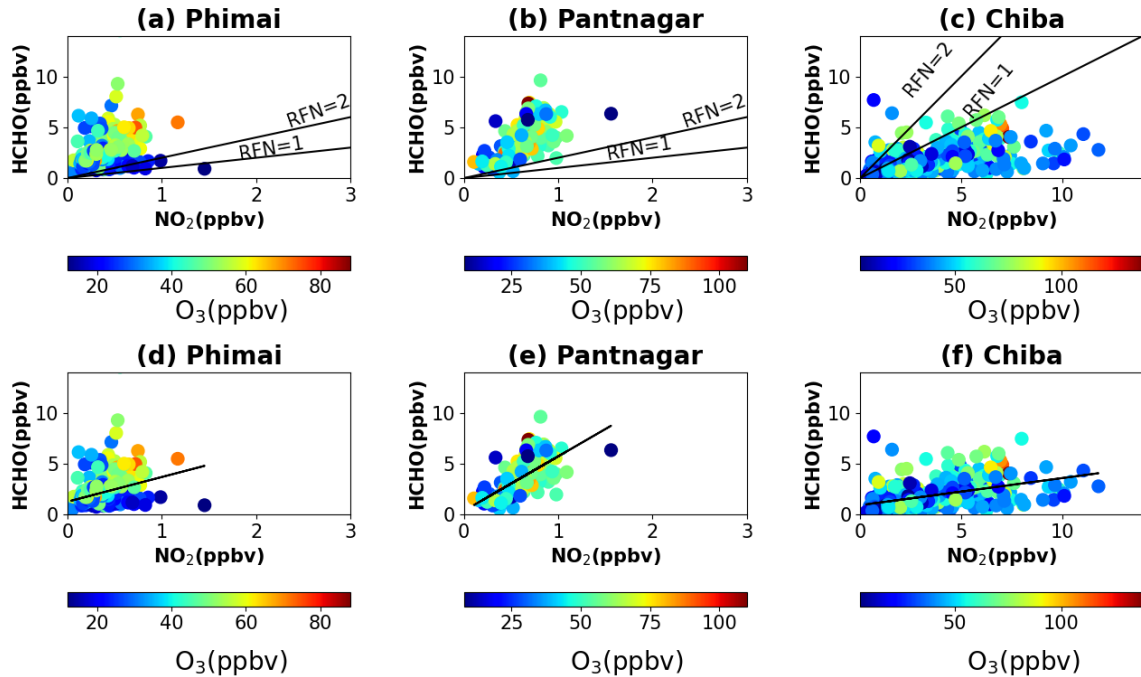
The HCHO to NO₂ (R_{FN}) ratio is regarded as an indicator of high ozone O₃ sensitivity (Martin et al., 2004; Duncan et al., 2010). The O₃ production regime is characterized as VOC-limited for $R_{FN} < 1$ and NO_x-limited when $R_{FN} > 2$, and the values in the range 1-2 are said to be in the transition/ambiguous region (Duncan et al., 2010; Ryan et al., 2020). Subsequent to a report of Tonnesen and Dennis (2000), several studies used R_{FN} estimated from satellite and ground-based observations to infer O₃ sensitivity to NO_x and VOCs (Martian et al., 2004; Duncan et al., 2010; Jin and Holloway et al., 2015; Mahajan et al., 2015; Irie et al., 2021; etc.). However, the effectiveness of R_{FN} is still under discussion primarily based on two-points- (1) the range of the transition region to categorize the VOC and NO_x -limited region, and (2) the altitude dependence of R_{FN} (Jin et al., 2017). Most of the studies described above used the transition range ($1 < R_{FN} < 2$) proposed by Duncan et al. (2010). Schroeder et al. (2017) reported that a common transition (i.e., $1 < R_{FN} < 2$) range might not be valid globally. Instead, it should be calculated based on the region. First, the results based on the standard transition range are discussed herein, and then its applicability to the study regions is assessed.

Figure 5 shows scatter plots of the daily mean NO₂ and HCHO concentrations in the 0 - 2 km layer at the three sites, color-coded with the respective O₃ concentrations (0-2 km). Retrieval of the JM2 O₃ product is explained by Irie et al. (2011). The O₃ concentrations for SZA < 50° are used to minimize stratospheric effects. This criterion on the SZA is also applied for the selection of the NO₂ and HCHO concentrations. Although not checked here, the JM2 O₃ product showed good agreement with ozonesonde measurements in Tsukuba (Irie et al., 2021). Most of the high O₃ occurrences fall in the $R_{FN} > 2$ region at Phimai and Pantnagar and in $R_{FN} < 1$ at Chiba. The common transition range classifies the O₃ production regime as

NO_x-limited at Phimai and Pantnagar and VOC-limited at Chiba. At all sites, the R_{FN} values tend to be biased to a particular regime (i.e., NO_x - or VOC-limited), with only 4 and 2% of the ratios in the range 0 - 2, at Phimai and Pantnagar, respectively. This finding suggests that the transition occurs at a higher or lower ratio than the common definition. Recent report by Souri et al. (2020) found that the NO₂-HCHO relation plays an important role in determining the transition region and derived a formulation from accounting for the NO₂-HCHO chemical feedback in the ratios as

$$HCHO = m * (NO_2 - b) \quad (6)$$

where m and b respectively denote the slope and intercept. Equation (6) is based on observations, which means that the regionally adjusted fitting coefficients will reflect the local NO₂ - HCHO relation. Solving equation (6), the transition line estimated from the observations in the 0 - 2 km layer, is shown in Fig 5 (bottom panel). Rather than a range, the method calculates a single transition line, which corresponds to the NO₂ - HCHO feedback. The regions above and below the transition line are characterized, respectively as VOC- and NO_x -limited or other.



481 **Figure 5.** Scatter plots of HCHO and NO₂ concentrations in the 0-2 km layer at (a, d) Phimai, (b, e) Pantnagar, and
482 (c, f) Chiba, coloured with the O₃ concentrations in the 0-2 km layer at the respective sites. The solid lines in the
483 top panel represent $R_{FN} = 2$ and $R_{FN} = 1$ benchmarks. The black lines in the bottom panel are calculated according
484 to equation (1).

485

486 The revised transition line at Phimai and Pantnagar is apparently more reasonable than the earlier method.
487 At Phimai, the transition line almost clearly distinguishes between the high and low O₃ occurrences. It is
488 perceptible that when the HCHO concentrations are higher than NO₂, the transition of the regimes is likely
489 to occur at higher R_{FN} values. The minimum and mean R_{FN} value along the transition line are 3.62 and
490 6.78, respectively. Because Phimai is a VOC-rich environment, the regime transition occurs at higher R_{FN}
491 values than by the conventional definition. This finding echoes the results reported by Schroeder et al.
492 (2017) for a regionally variable transition region. The definition of $R_{FN} < 1$ as a VOC -limited regime might
493 not be valid in this case. Considering the mean R_{FN} ratio along the transition line (i.e., 6.78), the VOC-
494 and NO_x -limited (and other) regimes are defined, respectively as $R_{FN} < 6.78$ and $R_{FN} > 6.78$. Based on this
495 definition, around 34% (65%) of the ratios are higher (lower) than 6.78, classifying Phimai as a dominant
496 VOC-limited region, which contradicts earlier results. Biomass burning affects Phimai during January -
497 April and is a significant emission source in addition to biogenic emissions. Thus, high O₃ occurrences
498 likely occur only 30% of the time during a year. Such events mostly lie above the transition line.

499 At Pantnagar, high O₃ occurrences lie below (42%) and above (57%) the transition line, indicating that
500 O₃ production is sensitive to both HCHO and NO₂ which contradicts results reported by Biswas et al.
501 (2019). Based on satellite and ground-based observations, the study estimated the R_{FN} values at a site in
502 the IGP as > 4 and > 2 respectively, and regarded the O₃ regime as NO_x-limited. Mahajan et al. (2015)
503 reported R_{FN} values of less than 1 over the IGP region signifying as a VOC-limited region. Pantnagar is
504 a sub-urban site situated beside a busy road. Therefore, effects of anthropogenic emissions are expected
505 year-round, especially with pyrogenic emissions during the spring and post-monsoon period. O₃
506 sensitivity to both NO_x and VOCs in the north-west IGP region has also been reported by Kumar and
507 Sinha (2021). Therefore, the balance between the VOC and NO_x-limited region in the IGP is reasonable.
508 The mean and minimum R_{FN} value along the transition line are, respectively, 5.59 and 6.09. The minimum

509 value (i.e., 5.59) is higher than Phimai (3.26), suggesting higher VOC levels at Pantnagar, consistent with
510 the observations.

511 At Chiba, 60% of the R_{FN} values lie below the transition line, suggesting a dominant VOC-limited
512 region, which is consistent with the results reported by Irie et al. (2021). The minimum and the mean R_{FN}
513 along the transition line are, respectively, 0.33 and 0.72. The transition occurs at a low R_{FN} value because
514 of higher NO_2 levels. The fact that, 40% of the R_{FN} values are above the transition region suggests a
515 moderate effect of HCHO on the O_3 sensitivity at Chiba.

516 Although the new classification results are apparently reasonable, they should be interpreted with
517 care. Our current understanding of R_{FN} contradicts the classification of rural sites as VOC-limited. Despite
518 the theoretical and observational evidence (i.e., Souri et al., 2020), the classification of regimes based on
519 a single transition line is not yet well-established. Schroder et al. (2017) used regionally varying transition
520 ranges. Moreover, (a) the number of observations and (b) the systematic and retrieval errors can affect
521 the estimations and classifications. These findings are expected to contribute to the ongoing discussion
522 about the effectiveness of R_{FN} . However, the results support the idea of a regionally varying transition
523 range.

524

525 3.1.3.2 R_{FN} profiles

526 Figure 6 shows the seasonal mean R_{FN} profiles at the three sites. Only the profiles during the high O_3
527 concentrations at the sites (i.e., March at Phimai, May at Pantnagar, and February at Chiba) are shown.
528 The R_{FN} values are likely increase with height because of the lower vertical gradient of NO_2 , than that of
529 HCHO (Fig.4). It is particularly interesting that, the R_{FN} values are similar in the 1-2 km height under
530 biomass burning conditions, suggesting a small variation in the HCHO loss rate in the particular layer. At
531 both sites, the HCHO concentration at 1.5 km is about 3 ppbv. At Chiba, a considerable amount of NO_2
532 in the higher layers increases the ratio up to 2 km height. Beyond 2 km, the ratio variation at all sites is
533 opposite that found for the surface. The gradient issue of R_{FN} has been discussed explicitly by Jin et al.
534 (2017). They proposed a conversion factor to account for gradient differences in the surface and column-
535 derived R_{FN} values, estimating the conversion factor from the model simulated surface and column

536 abundances of NO₂ and HCHO. We adopt the method reported by Jin et al. (2017) for this study using
537 the CHASER simulated NO₂ and HCHO concentrations and vertical columns.

538 First, CHASER simulated near-surface NO₂ and HCHO concentrations were converted to number
539 density. The effective boundary layer height (E) (Halla et al., 2011; Jin et al., 2017) was estimated.

540

$$541 \quad E_{NO_2} = \frac{NO_2 \text{ total column}}{NO_2 \text{ near-surface number density}} \quad (7)$$

542

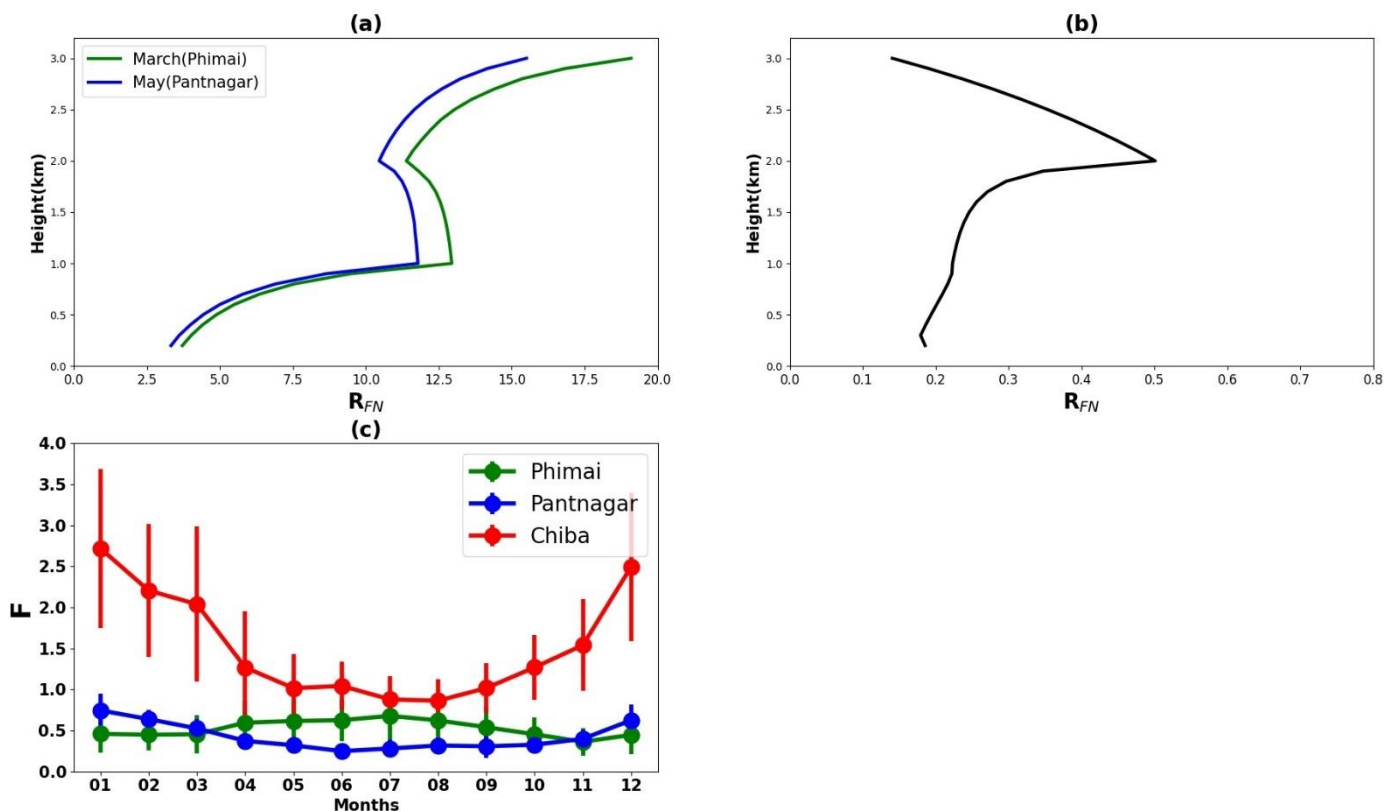
$$543 \quad E_{HCHO} = \frac{HCHO \text{ total column}}{HCHO \text{ near-surface number density}} \quad (8)$$

544 Therein, E_{NO₂} and E_{HCHO} respectively denote the effective boundary layer heights of NO₂ and HCHO.

545 In the second step, the column to surface conversion factor (F) was calculated according to the following
546 equation:

$$547 \quad F = \frac{E_{HCHO}}{E_{NO_2}} \quad (9)$$

548 The seasonal variation of F for the three A-SKY sites and the associated 1σ standard deviation of the
549 mean values are depicted in Fig. 7(c). The F values over East Asia reported by Jin et al. (2017) were ~2,
550 without marked seasonal variation. CHASER estimated F values over Chiba range between 1–2.5, which
551 is apparently reasonable, when compared with literature values. Values reported in literature for polluted
552 regions (NO₂ > 2.5 molecules cm⁻²) considered simulation data for 1–2 PM, but the estimates for this
553 study used daytime (07:00 – 18:00) simulations.



554

555 **Figure 6:** Seasonal mean R_{FN} profiles during (a) March and May at Phimai and Pantnagar, respectively, and (b)
 556 February at Chiba. (c) Seasonal variations in the column to surface conversion factor (F) for the Phimai, Pantnagar,
 557 and Chiba sites, estimated from the CHASER simulated HCHO and NO₂ surface concentrations and VCD. The
 558 simulated data from 07:00 – 18:00 in 2017 were used to estimate the F values. The error bars represent the one
 559 sigma standard deviation of the mean values.

560

561 The F values for Pantnagar are mostly less than 1, with no distinctive seasonal variation. Mahajan et
 562 al. (2015) reported OMI-derived R_{FN} values < 1 over the IGP region. When this estimated conversion
 563 factor is used with the values reported by Mahajan et al. (2015), the discrepancy in the satellite and
 564 ground-based observation derived R_{FN} values in the IGP region are reduced indicating that the estimated
 565 F values for the Pantnagar site can be representative for the IGP region. The F values at the Phimai site

range were 0.5–1. Our estimated F values for the Phimai and Pantnagar sites are useful as representative values for these respective regions, which can be improved further based on the results.

3.2 Global Evaluation of the CHASER model

This section describes the evaluation of CHASER NO₂ and HCHO columns for 2017 against OMI observations. The OMI AKs were applied to the CHASER outputs to account for the altitude-dependence of the retrievals. First, 2-hourly simulated profiles (NO₂ and HCHO) were sampled closest to the observation time. Secondly, AKs were applied to the sampled profiles and the mean profile was calculated. Thirdly, both the simulations and observations were averaged on a 2.8° bin grid. The month of July and December were discarded from the NO₂ comparison because few coincident days (only five days) were available after filtering. It should be noted that simulations based on old NO_x emission inventory will likely affect the model-satellite comparison results. However, the current study has not assessed such impact due to technical issues related to using an updated emission inventory. All these issues will be addressed in a separate study.

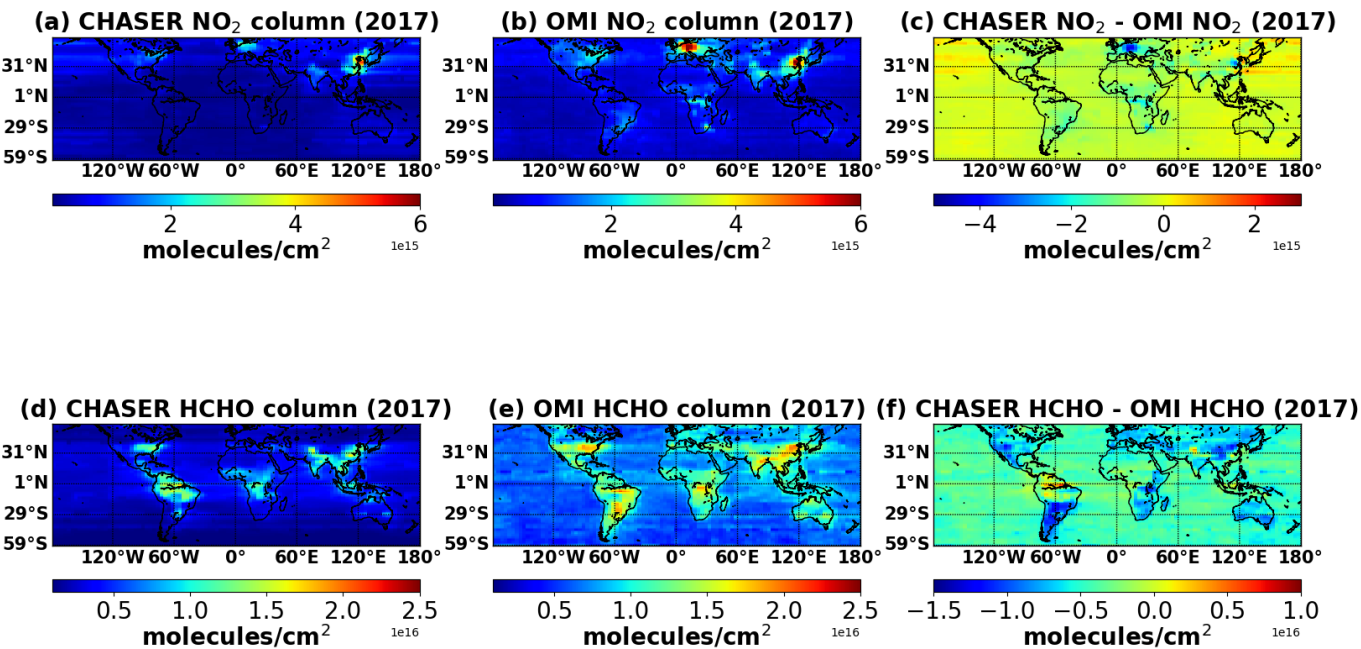
3.2.1 Comparison between CHASER and OMI NO₂

Figure 7 compares the simulated and observed annual mean tropospheric NO₂ columns. The statistics for the comparison are given in Table 5. The model captured the global spatial variation well with a spatial correlation (r) of 0.70. The mean bias error (MBE) and the root mean square error (RMSE) are respectively, 3×10^{14} and 5.4×10^{14} molecules cm⁻². On a global scale, CHASER estimations are negatively biased by 38% compared to OMI. Actually, studies evaluating global NO₂ simulations with satellite observations have reported similar negative biases (Miyazaki et al., 2012, Sekiya et al., 2018). The differences in the spatial representativeness between the model and observations is one potential reason for such negative biases. CHASER simulations at 1.1° improved the MBE and RMSE by 5 and 15%, respectively, compared to simulations at 2.8° (Sekiya et al. 2018). Moreover, Sekiya et al (2018) used NO₂ simulations with an updated inventory and compared the results with OMI observations from 2014. Although they reported a better global spatial correlation ($r > 0.90$), the MBE (2.5×10^{14} molecules cm⁻²) and RMSE (4.4×10^{14} molecules cm⁻²) values at 2.8° resolution are comparable to those obtained from this study.

594 OMI retrievals show the highest NO₂ columns over eastern China (E-China) and Western Europe. Annual
595 mean NO₂ columns over the remainder of the land areas are between 7×10^{14} and 4×10^{15} molecules cm⁻².
596 Over the land areas the differences between the datasets are mostly between -2×10^{15} and 5×10^{14} molecules
597 cm⁻². Although CHASER also underestimates NO₂ columns over the ocean, the differences are lower than
598 that of over lands. CHASER estimates are higher by $\sim 5 \times 10^{14}$ molecules cm⁻² than OMI over Japan. Since
599 2012, the NO₂ columns have shown a declining trend over Japan, mainly because of emission controls in
600 China (Irie et al 2016). Probably because of simulations with an emission inventory earlier than 2012, the
601 simulated values tend to be higher than observations.

602 Figure 8 compares the seasonal variations in the monthly mean NO₂ columns in some selected region.
603 The error bars represent the 2-sigma standard deviation of the observed mean values. The numbers in
604 each subplot signify the regional spatial correlation between the datasets. Over eastern China (E-China),
605 CHASER values are negatively biased by 24%; the *r*-value is 0.68. The model captured the seasonality
606 well within variation range of the observations. Over E- and W-USA (eastern and western USA), the
607 respective *r*-values are 0.85 and 0.49 respectively. Simulated NO₂ columns are higher over E-USA than
608 over W-USA, consistent with the observations. Although, in both regions model estimates are biased by
609 $\sim 23\%$ in the lower side compared to OMI observations, the RMSE in E-USA are $\sim 40\%$ higher than in W-
610 USA.

611 Over Europe, CHASER estimates are negatively biased by 54%, with an *r*-value and RMSE of 0.80 and
612 1.28×10^{15} molecules cm⁻², respectively. The observed NO₂ levels over Europe are almost twice those of
613 the W-USA. The model was unable to capture the regional differences. Model underestimations in Europe
614 can be attributed to the older anthropogenic emission inventory used for the study. In fact, using the HTAP
615 2010 inventory the MBE (-0.53×10^{15} molecules cm⁻²) between OMI and CHASER NO₂ column
616



618 **Figure 7:** (top panel) Annual mean tropospheric NO₂ ($\times 10^{15}$ molecules cm⁻²) columns (a) simulated by CHASER
619 and (b) retrieved from OMI observations. Limited NO₂ data in July and December met the filtering criteria, thus
620 discarded from the calculation. (c) The differences between the simulated and observed NO₂ columns. (bottom
621 panel) Annual mean HCHO ($\times 10^{16}$ molecules cm⁻²) columns (d) simulated by CHASER and (e) retrieved from
622 OMI observations. (f) The differences between the simulated and observed HCHO columns. The data for 2017 are
623 plotted only. All the datasets are mapped onto a 2.8° bin grid.

624
625 simulations at 2.8 over Europe (Sekiya et al. 2018) was ~ 50% lower than in the current study, although
626 their RMSE value is similar.

627 Over India, MBE and RMSE for the annual mean NO₂ column are -4.3×10^{14} and 4.4×10^{14} molecules
628 cm⁻², respectively, and the *r*-value is moderate (0.65). Although CHASER estimates are negatively biased
629 by
630
631
632 **Table 5:** Statistics of comparison of annual mean NO₂ and HCHO columns between CHASER and OMI. MBE1
634 and MBE2 are the respective mean bias error. RMSE1 and RMSE2 are the respective root mean square errors. *r*₁
635 and *r*₂ signifies the respective spatial correlation coefficient. The units of MBE1 and RMSE1 are $\times 10^{15}$ molecules
636 cm⁻². MBE2 and RMSE2 values are in the unit of $\times 10^{16}$ molecules cm⁻².

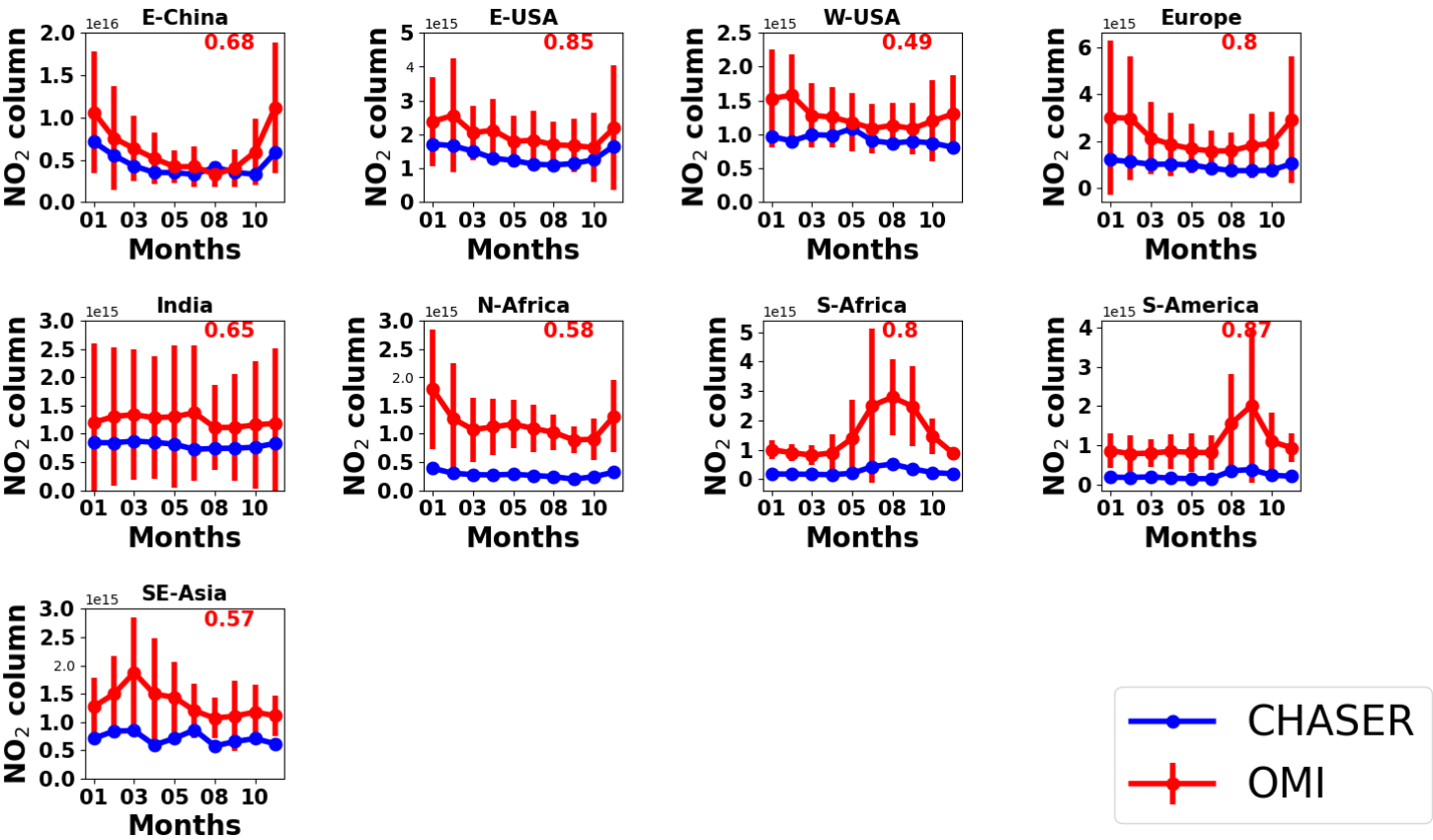
| Region | r ₁ (CHASER vs OMI NO ₂) | MBE1 (CHASER - OMI NO ₂) | RMSE1 (CHASER – OMI NO ₂) | r ₂ (CHASER vs OMI HCHO) | MBE2 (CHASER – OMI HCHO) | RMSE2 (CHASER – OMI HCHO) |
|-----------|--|--|--|--|-----------------------------------|------------------------------|
| Global | 0.73 | -0.30 | 0.54 | 0.74 | - 0.45 | 0.49 |
| E-China | 0.68 | -1.84 | 2.47 | 0.57 | -0.63 | 0.64 |
| E-USA | 0.85 | -0.62 | 0.63 | 0.91 | -0.56 | 0.56 |
| W-USA | 0.49 | -0.33 | 0.37 | 0.63 | -0.71 | 0.71 |
| Europe | 0.80 | -1.20 | 1.28 | 0.51 | -0.67 | 0.68 |
| India | 0.65 | -0.43 | 0.44 | 0.73 | -0.56 | 0.57 |
| N-Africa | 0.58 | -0.88 | 0.90 | 0.65 | -0.29 | 0.32 |
| S-Africa | 0.80 | -1.25 | 1.40 | 0.22 | -0.66 | 0.70 |
| S-America | 0.87 | -0.80 | 0.88 | 0.47 | -0.31 | 0.40 |
| SE Asia | 0.57 | -0.61 | 0.64 | 0.48 | -0.41 | 0.44 |

637
638

639 32%, the values lie within the 2-sigma range of the observations. Sekiya et al. (2018) found no significant
640 effect of higher model resolution on the MBE and RMSE in the Indian region.

641 Over N- and S-Africa (North and South Africa), the model values are biased low by more than 75%
642 compared to the observations. Prominent biomass burning occurs in both regions, which explains the
643 enhanced NO₂ levels in the OMI retrievals. High negative biases in the model values indicates that
644 biomass burning NO_x emissions for the African regions are likely underestimated. Similarly, CHASER
645 underestimates NO₂ columns by 80% in South America, where pyrogenic emissions contributions are
646 significant. CHASER estimates are lower than OMI in these regions, but model captured the spatial
647 distribution well.

648 Over the SE-Asian (Southeast) region, OMI columns are enhanced during the dry season (i.e., January -
649 April. Burning agricultural wastes is a common practice in many countries in Southeast Asia during the
650 dry season, explaining the enhanced columns. The MBE (-6×10^{14} molecules cm⁻²) and RMSE ($6.4 \times$
651 10^{14} molecules cm⁻²) in the SE-Asia region are lower than the African regions (i.e., N-Africa, S-Africa,
652 and S-America), where biomass burning is prominent.



654

655 **Figure 8:** Seasonal variations in tropospheric NO₂ columns in E-China (110° -123° E, 30° – 40° N), E-USA (32°
656 – 43° N, 71° – 95° W), W-USA(32° – 43° N, 100° – 125° W), Europe (35° – 60° N, 0° – 30° E), India (7.5° – 54° N,
657 68° – 97° E), N-Africa (5° – 15° N, 10° W – 30° E), S-Africa (5° -15° S, 10° -30° E), S-America (0° -20° S, 50° -
658 70° W), and SE-Asia (10° – 20° N, 9° – 145° E). CHASER simulations and OMI retrievals are plotted in blue and
659 red colors respectively. The error bars indicate the 2-sigma variation of the observed mean values. The number in
660 the insets signifies the regional spatial correlation between CHASER and OMI NO₂ columns.

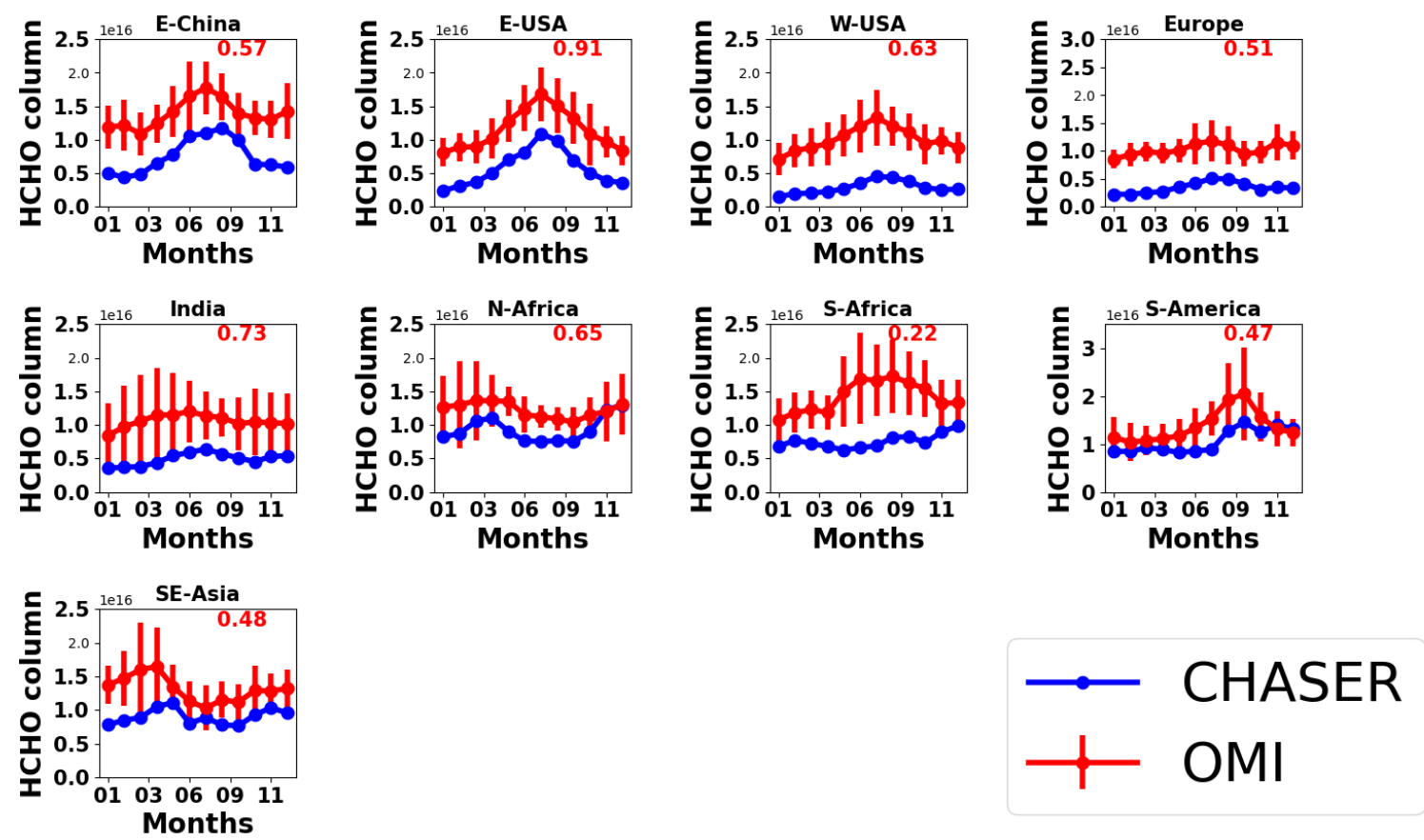
661

662 **3.2.2 Comparison between CHASER and OMI HCHO**

663 **Figure 9** presents a comparison between the simulated and observed global annual mean HCHO columns.
664 The statistics of the comparison are given in Table 5. CHASER is able to reproduce the observed global
665 spatial variation well with $r = 0.73$. The global MBE and the RMSE are respectively, -4.5×10^{15} and 4.9

666 $\times 10^{15}$ molecules cm^{-2} . MBE and RMSE for monthly mean fields show no distinctive seasonal variation
 667 (Table S2). High HCHO columns are observed over China, Australia, Europe, India, Central Africa, South
 668 America, and the United States. The model mostly underestimated the HCHO abundances in the higher
 669 latitudes and Australia. Absolute differences between the model and observations in the higher latitudes
 670 vary between 5×10^{15} and 1×10^{16} molecules cm^{-2} . Figure 9 compares the seasonal variations in the monthly
 671 mean HCHO columns in some selected region. Therein error bars represent the 2-sigma standard
 672 deviation of the observed mean values. The numbers in the respective subplots signify the regional spatial
 673 correlation between the datasets.

674 Over E-China, CHASER HCHO estimates are negatively biased by 45% compared to OMI and the r -
 675 value is greater than 0.50. The model reproduced the observed HCHO seasonality well including
 676 enhanced peaks during the summer. The greatest differences between the datasets are observed during
 677 the winter. Over E-USA, the spatial correlation between the datasets is greater than 0.90. Also, the
 678 CHASER estimates are biased by 49% in the lower side. Simulations show that the peak in the HCHO
 679 abundances occurs in July, which is consistent with the observations. The observed and simulated
 680 magnitude of the seasonal modulation is 51 and 78%, respectively. The seasonality in the HCHO columns
 681 in E-China and E-USA signifies a strong contribution from biogenic emissions. In both regions, the
 682 observed peak HCHO column is $\sim 1.75 \times 10^{16}$ molecules cm^{-2} . The simulated peak HCHO values are also
 683 similar in both regions, despite the underestimation. Over W-USA and Europe, the negative biases in the
 684 simulation are greater than 60%. However, the simulated peaks during summer are consistent with the
 685 observations. The OMI retrievals show that the HCHO abundances in both regions are almost similar,
 686 which has been well captured by CHASER, although the magnitude is underestimated.



689 **Figure 9:** Seasonal variations in HCHO columns in E-China (110° - 123° E, 30° - 40° N), E-USA (32° - 43° N,
690 71° - 95° W), W-USA(32° - 43° N, 100° - 125° W), Europe (35° - 60° N, 0° - 30° E), India (7.5° - 54° N, 68° -
691 97° E), N-Africa (5° - 15° N, 10° W - 30° E), S-Africa (5° - 15° S, 10° - 30° E), S-America (0° - 20° S, 50° - 70° W),
692 and SE-Asia (10° - 20° N, 9° - 145° E). CHASER simulations and OMI retrievals are plotted in blue and red colors
693 respectively. The error bars indicate the 2-sigma variation of the observed mean values. The number in the insets
694 signifies the regional spatial correlation between CHASER and OMI HCHO columns.

696 Over India, the model estimates mostly lie outside of the observational variation ranges, although,
697 CHASER captured the spatial distribution well ($r = 0.73$). Magnitudes of the seasonal variation in both
698 OMI and CHASER are around 32%. Between the two African regions, CHASER demonstrated better
699 capability for reproducing HCHO distribution in N-Africa ($r = 0.65$). Negative model bias in N-Africa is

almost half (22%) that of S-Africa (46%). Observed N-African HCHO columns are mostly higher than
 1.2×10^{16} molecules cm^{-2} during the biomass burning period (November - April). Although the modeled
 values are lower than the observed values, the year-end columns (November - December) are similar.
 Both datasets show low HCHO variation during May - September. Over the S-African region, the model
 capabilities were limited.

Over S-America, the negative bias (~22%) in the model estimates compared to the observations is similar
 to that of N-Africa. In addition to consistency in the year-end (November to December) columns,
 CHASER well reproduced the biomass burning-led enhancements. The observed and simulated
 magnitudes of seasonal modulation are 49 and 43%, respectively.

Over SE-Asia, CHASER reproduced the observed biomass burning-led enhanced HCHO columns during
 the dry season (January - April), however, the occurrence of the peak is inconsistent. As discussed in
 section 3.1, observed HCHO peaks related to biomass burning can vary depending on the fire numbers.
 The r -value (0.48) is moderate and model is biased by 30% in the lower side. The model negative biases
 in the biomass prone regions are lowest (<30%) among the discussed regions.

De Smedt et al. (2021) reported that cloud corrections can positively bias OMI HCHO columns up to
 30% compared to Tropospheric Ozone Monitoring Instrument (TROPOMI) columns. Consequently,
 uncertainties in the observations are also likely to contribute to the observed negative biases. Comparison
 among CHASER, TROPOMI, and OMI HCHO columns is beyond the scope of this study. However, the
 effects of uncertainties in the satellite retrievals on the negative biases is discussed qualitatively and
 briefly. To demonstrate such effects, CHASER and TROPOMI HCHO columns for 2019 are compared
 in Fig S3. The simulation settings and emission inventories are similar to those explained in section 3.2.3.

The comparison results are presented in Table S2. TROPOMI data has been processed following De
 Smedt et al. (2021). The CHASER and TROPOMI HCHO spatial distribution correlates strongly with r -
 value of 0.78. The values for MBE and RMSE are respectively, -2.3×10^{15} and 2.8×10^{15} molecules cm^{-2} .
 Compared to OMI and TROPOMI, CHASER HCHO columns are negatively biased, respectively, by
 61 and 38%. The model biases are lower when compared to TROPOMI observations. Because of temporal
 differences in the two comparisons, the biases cannot be compared quantitatively. However, the
 differences in the biases signify that the observational uncertainties can strongly affect discrepancies

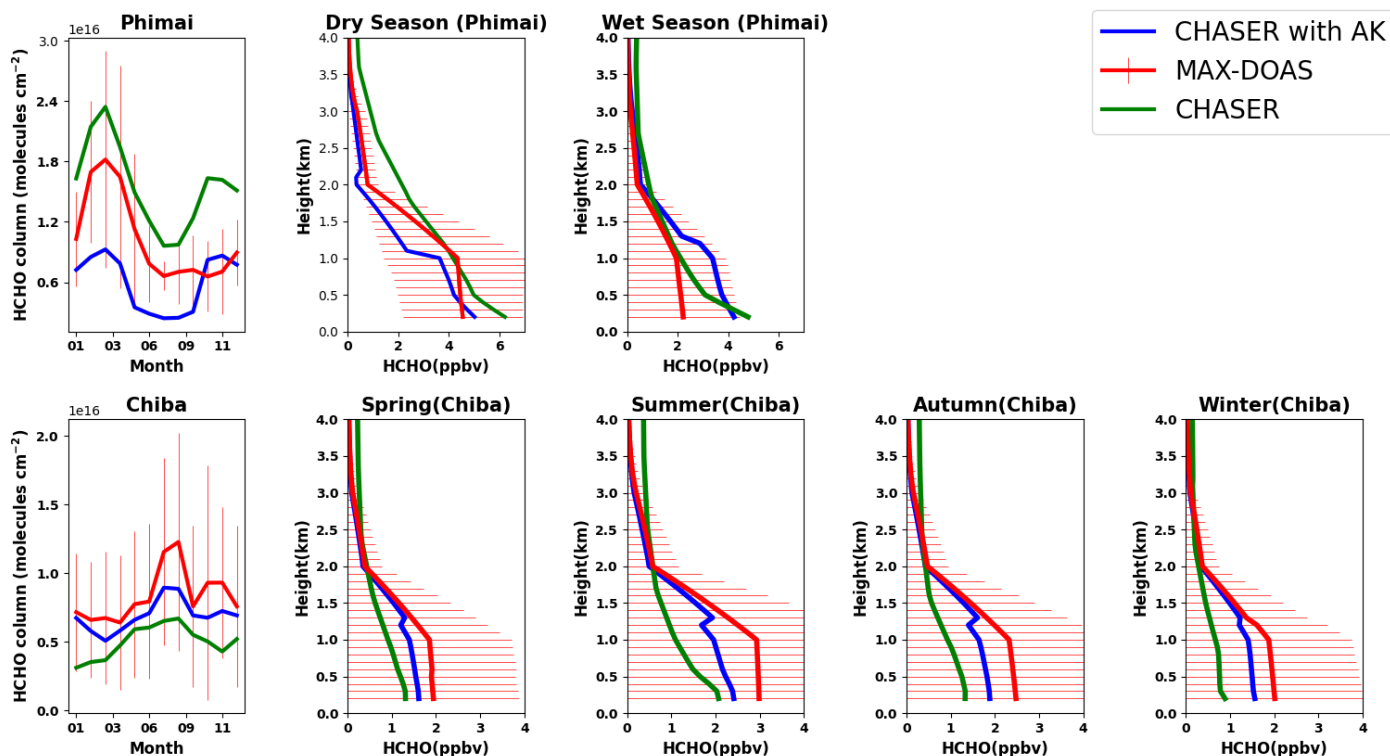
between the simulated and observed HCHO abundances. Moreover, using different cloud products may introduce inconsistencies in the OMI BIRA-IASB retrievals (De Smedt et al., 2021), affecting the comparison results. De Smedt et al. (2021) proposed to recalculate the OMI HCHO VCDs based on the AMF information to minimize cloud-induced uncertainties. Such a detailed method will be evaluated in our future studies.

3.3 Evaluation of CHASER simulations at the three sites

3.3.1 Evaluation of CHASER HCHO at Phimai and Chiba

The seasonally averaged observed and modeled HCHO profiles and partial columns in the 0 - 4 km altitude range at Phimai and Chiba are presented in Fig. 10. The CHASER outputs smoothed with MAX-DOAS averaging kernels (AK) are also depicted. The AK is applied following Franco et al. (2015). First, the CHASER HCHO profiles are interpolated to the MAX-DOAS vertical grids. Next, the MAX-DOAS AK information from individual retrieved profiles is seasonally averaged according to the climate classifications of each site. Finally, the CHASER outputs on the coincident days are selected, and the seasonally averaged AK is applied to the daily mean interpolated profile. Applying individual AKs to the model outputs yielded similar results. The seasonally averaged AKs for both sites are shown in Fig S4. The coincident days at Phimai and Chiba were respectively, 690 and 668.

At Phimai, CHASER predicted the increase in the HCHO partial columns during the dry season and well-reproduced the HCHO seasonality. The simulated and observed seasonality correlates strongly with R -value of 0.96. The modeled monthly mean values during the dry season are found to be within the 1σ standard deviation of the observed values, indicating that the pyrogenic emissions estimates used for the simulations are reasonable. CHASER predicted a 41% increase in the HCHO column during January - March, consistent with the observations (41%). CHASER overestimates the HCHO columns in both seasons, and the mean bias error (MBE) (CHASER – MAX-DOAS) is lower (3.7×10^{15} molecules cm^{-2}) (Table 6) during the wet season. Although underestimated, the dry season smoothed column values are within the 1σ range.



755 **Figure 10.** Seasonal variations in the HCHO partial columns at 0 - 4 km and vertical profiles during all seasons at
 756 Phimai and Chiba, as inferred from the MAX-DOAS observations (red) and CHASER simulation (green). The
 757 CHASER HCHO partial column and vertical profile smoothed with the MAX-DOAS AK are coloured blue. The
 758 AK information of all the screened (as explained in section 2.2) retrievals were averaged based on the seasonal
 759 classification of the respective sites. The coincident time and date between the model and observations are selected
 760 only. Error bars indicate the one sigma standard deviation of mean values of the MAX-DOAS observations.

761
 762 The modeled and observed HCHO mixing ratios in the 1- 2km layers during the wet season are almost
 763 identical, whereas VMR near the surface (i.e., 0 - 1 km) differ by 30%. The absolute mean difference in
 764 the 0-4 km layer is ~0.45ppbv, with the maximum difference of 2.58 ppbv below 200 m. CHASER has
 765 demonstrated good capabilities for reproducing the HCHO profile in the 0.5 – 4 km layer during the wet
 766 season. The significance of AK information is low for the wet season. However, smoothing the model
 767 profiles reduces the overall MBE by 43%.

768

Table 6: Comparison of the seasonal mean HCHO partial columns and profiles (0-4 km) between MAX-DOAS and CHASER at Phimai and Chiba. MBE (CHASER – MAX-DOAS) is the mean bias error. The partial column and profile MBE units are respectively, $\times 10^{16}$ molecules cm^{-2} and ppbv, respectively.

| Site | Season | Partial column MBE | Smoothed Partial column MBE | Profile MBE | Smoothed Profile MBE |
|--------|---------|--------------------|-----------------------------|-------------|----------------------|
| Phimai | Overall | 0.28 | -0.07 | 0.35 | 0.01 |
| Phimai | Dry | 0.37 | -0.28 | 0.58 | -0.38 |
| Phimai | Wet | 0.21 | 0.07 | 0.45 | 0.33 |
| Chiba | Overall | -0.12 | -0.05 | -0.37 | -0.11 |
| Chiba | Spring | -0.07 | -0.04 | -0.22 | -0.12 |
| Chiba | Summer | -0.16 | -0.08 | -0.45 | -0.26 |
| Chiba | Autumn | -0.10 | -0.04 | -0.40 | -0.19 |
| Chiba | Winter | -0.09 | -0.01 | -0.42 | 0.11 |

During the dry season, the respective absolute mean and maximum difference in the datasets in the 0 -1 km layers is ~1 and ~2ppbv. The observed and simulated seasonal differences in the 0-1 km are 50 and 34%, respectively. Simulated dry season profile values at the heights greater than ~2 km is out of the 1σ variation range. The two-potential reasons for such differences are lower measurement sensitivity in the free troposphere and the overestimated Southeast Asian biogenic emissions in the model. Despite the measurement limitations, CHASER and MAX-DOAS wet season profiles up to 3 km are consistent. Consequently, it is likely that the biogenic emissions for this region in the model are overestimated. The Southeast Asian isoprene emissions in CHASER is 128 Tgyr^{-1} , higher than the CMAS-GLO-BIO (Sindelarova et al., 2022) inventory (78 Tgyr^{-1}). However, the dry season HCHO profiles in 0 - 2 km are well simulated. Smoothing underestimates the dry season profile within the 1σ variation range but improved simulations below 200 m. At heights greater than 3 km, the smoothed values mostly reproduce the a priori because of reduced measurement sensitivity (i.e., low AK value, indicating limited information was retrievable).

788 Moderate correlation ($R=0.58$) can be observed between the modeled and observed HCHO partial
789 columns at Chiba. CHASER was able to reproduce the peak in the partial columns in August. The model
790 predicts a 41% increase in the HCHO columns during January - August, whereas the observed increase
791 is 54%. Although Chiba is an urban site, the HCHO and temperature seasonal variations show a tight
792 correlation ($R\sim 0.70$) (Fig S5), suggesting that changes in biogenic emissions modulate HCHO
793 seasonality. Similarly, the modeled seasonality is consistent with temperature variation (Fig. S4). Thus,
794 the simulated HCHO seasonality in Chiba is reasonable, despite underestimation of absolute values.
795 Smoothing the simulations improve the correlation, and the MBE is reduced by 54% (Table 6).

796 The CHASER HCHO profiles in the 0 - 4 km layers are lower than the observations, with an MBE
797 of 0.39 ppbv. The absolute differences in the modeled and retrieved HCHO profiles in the 0-2 km layer
798 during all seasons are higher than at Phimai. Absolute mean differences of ~ 1 ppbv and higher are mainly
799 observed for 0 to 2 km. In addition, the vertical gradients of the simulated profiles are low compared to
800 those at Phimai. The modeled profiles at Chiba resemble the HCHO profiles measured over the ocean
801 during the INTEx-B (Intercontinental Chemical Transport Experiment: Phase B) (Boeke et al., 2011).
802 The Chiba site is near the sea, and coarse CHASER resolution includes the ocean pixels. Moreover, urban
803 surfaces are not homogeneous. Thus, a significant part of the profile discrepancies is likely related to the
804 systematic differences, in addition to emission estimates. However, the model estimates lie within the
805 standard deviation range of the measurements. Because of the low gradients in the simulated profiles, the
806 smoothed profiles mostly imitated the a priori values even below 2 km. Overall, given the large
807 uncertainty on the MAX-DOAS profiles (Fig. 10), the differences between the observations and smoothed
808 profile are statistically insignificant. Effects of the horizontal resolution on the simulated HCHO levels is
809 discussed in section 3.3.4.

810

811

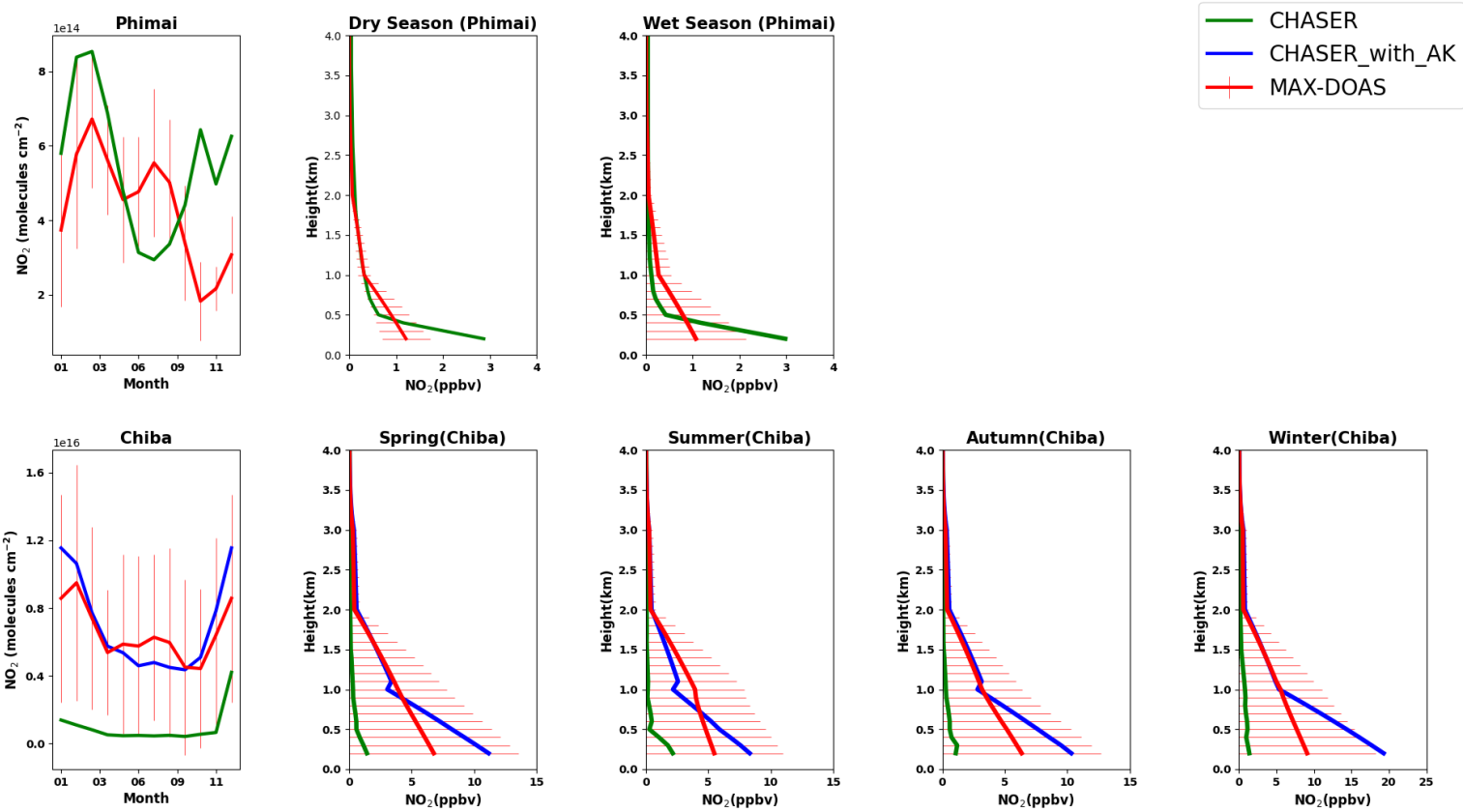
812 3.3.2 Evaluation of CHASER NO₂ in Phimai and Chiba

813 Figure 11 presents the seasonal averages of the MAX-DOAS and CHASER NO₂ profiles and partial
814 columns (0 - 4 km) at Phimai and Chiba. The AK is applied to the modeled outputs for the Chiba site
815 only.

816 Figure S5 of the supplementary information presents a comparison of the observations, model, and
817 smoothed model profiles averaged within the 0 - 2 km layer at Phimai. Smoothing with different a priori
818 values is depicted to demonstrate the effects of the a priori values. The smoothed NO₂ concentrations,
819 calculated using the original a priori values, show a seasonal variation shift. The mean smoothed profile
820 resembles the observations when a priori values are reduced by 50%; however, the dry season values are
821 similar in both cases. Two test cases of smoothing profiles using apriori values above 500 and 800 m
822 shows good agreement with the observations; however, the results are sensitive to the apriori values.
823 Because smoothed profiles are strongly biased to the apriori choice, the smoothing results obtained for
824 the Phimai site are discarded.

825 The modeled NO₂ partial column at Phimai shows good agreement with observations made during the
826 dry season. CHASER well reproduces the enhanced NO₂ columns attributable to biomass burning within
827 the standard deviation of the observations. The peak in the NO₂ levels during March is consistent in both
828 datasets. Although the seasonality does not agree in other months, the overall MBE is 8×10^{13} molecule
829 cm⁻² (Table 7). Above 500 m, the datasets shows excellent agreement. The absolute mean differences in
830 the 0 - 1km layer are 0.22 ppbv, and the maximum difference of ~1.9 ppbv is observed near the surface.
831 Amidst the biomass burning influence, the NO₂ concentrations at Phimai are mostly < 1 ppbv. Thus, the
832 results of comparisons demonstrate CHASER's good capabilities in regions characterized by low NO₂
833 concentrations. Moreover, when NO₂ concentrations are less than < 1 ppbv, the AK information seems
834 less significant if the model can capture low-concentration scenarios.

835



838 **Figure 11.** Seasonal variation in NO₂ partial columns from 0 - 4 km and vertical profiles during all seasons at
839 Phimai and Chiba, as inferred from the MAX-DOAS observations (red) and CHASER simulation(green). The
840 CHASER NO₂ partial column and vertical profile smoothed with the MAX-DOAS AK are coloured in blue. The
841 coincident time and date between the model and observations are selected only. The error bars represent the one
842 sigma standard deviation of mean values of the MAX-DOAS observations.

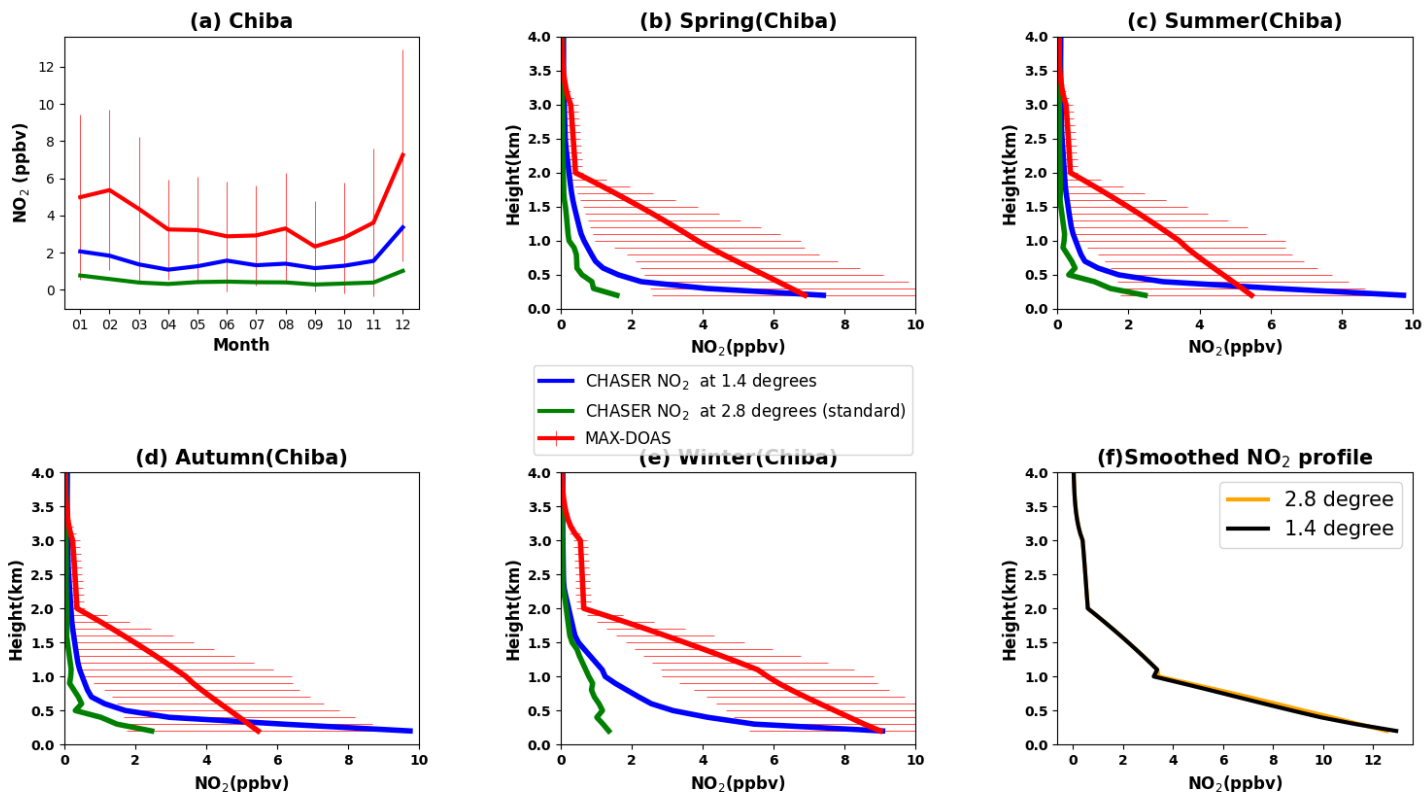
Table 7: Comparison of the seasonal mean NO₂ partial columns and profiles (0-4 km) between MAX-DOAS and CHASER at Phimai and Chiba. MBE (CHASER – MAX-DOAS) is the mean bias error. The partial column and profile MBE units are $\times 10^{15}$ molecules cm⁻² and ppbv, respectively.

| Site | Season | Partial column MBE | Smoothed Partial column MBE | Profile MBE | Smoothed Profile MBE |
|--------|---------|--------------------|-----------------------------|-------------|----------------------|
| Phimai | Overall | 0.08 | | 0.11 | |
| Phimai | Dry | 0.18 | | 0.09 | |
| Phimai | Wet | -0.14 | | 0.02 | |
| Chiba | Overall | -5.58 | -1.90 | -3.27 | -1.66 |
| Chiba | Spring | -5.56 | -2.00 | -3.19 | -1.74 |
| Chiba | Summer | -5.52 | -2.87 | -2.85 | -1.86 |
| Chiba | Autumn | -4.57 | -1.24 | -2.74 | -1.40 |
| Chiba | Winter | -6.64 | -1.50 | -4.30 | -1.63 |

Although the datasets are moderately correlated ($R=0.59$) at Chiba, the model largely underestimates the NO₂ partial column with MBE of $\sim 5 \times 10^{15}$ molecules cm⁻². The model predicts almost constant NO₂ profiles and columns throughout the year. Therefore, the respective seasonal biases are almost similar. The vertical gradient of the modeled NO₂ profiles is also low, too, similarly to the HCHO profiles. The model resolution can be a potential cause for such significant underestimation. The AKs improved the partial column and profiles significantly, reducing the MBE by more than 50%. However, the smoothed profiles and partial columns between the 0 - 2 km layer, differ significantly from the simulations, suggesting that the a priori values strongly affect the smoothed profiles. Consequently, the smoothed NO₂ profiles at Chiba (Fig.S7) are biased to the a priori values, similar to that of Phimai (Fig. S6). NO₂ smoothed profile sensitivity to a priori values might be attributable to our retrieval procedure. The a priori data are taken from the measured SCD and retrieved VCD values. As a result, the values are sensitive in the 0 - 2 km layer, similarly to the observations. Using a priori values other than those obtained from observations can affect such sensitivity. The smoothing sensitivity to a priori values is stronger for NO₂ than HCHO. The NO₂ profile gradient is higher than that of HCHO (Figs. 10 and 11), which means that,

866 within 10 km (MAX-DOAS horizontal resolution), the NO₂ mixing ratio and a priori variability (sources
867 and sinks) is higher than those of HCHO, leading to a stronger a priori effect on the smoothed profiles.
868

869 The mean NO₂ mixing ratios in the 0 - 2 km layer in 2018, simulated at spatial resolutions of $2.8^{\circ} \times 2.8^{\circ}$
870 (standard) and $1.4^{\circ} \times 1.4^{\circ}$, are compared with observations at Chiba, as depicted in Fig.12. The error bars
871 are the 1σ standard deviation of the observations. Higher resolution simulations reduced the overall MBE
872 by 35% (Table 8). NO₂ concentrations at 1.4° are now within the variation range of the observations. The
873 1.4° simulation captured the NO₂ seasonal variability better than at 2.8° . Despite improved resolution, the
874 model values are underestimated, with the highest MBE during the winter. According to Miyazaki et al.
875 (2020), the seasonality in the anthropogenic emissions, primarily wintertime heating, is not well
876 represented in the emission inventories, which could likely underestimate winter NO₂ levels. The best
877 agreement between the datasets is observed during summer and spring, with an MBE of ~1 ppbv on a
878 seasonal scale.
879



880 **Figure 12:** (a) Seasonal variations in the NO₂ mixing ratios in the 0 - 2 km layer at Chiba, as inferred from the
881 MAX-DOAS observations (red) and two CHASER simulations at 2.8°(green) and 1.4°(blue) resolutions. The
882 simulated NO₂ profiles at 2.8°(green) and 1.4°(blue) resolutions during (b) spring, (c) summer, (d) autumn, and (e)
883 winter are shown with the observed seasonal profiles at Chiba. Only data (both observed and simulated) for 2018
884 are plotted. The coincident time and date between the model and observations are selected only. The error bars in
885 (a), (b), (c), and (d) represent the one sigma standard deviation of mean values of the MAX-DOAS observations.

886

887

888 NO₂ profiles at 2.8° and 1.4° resolution are shown in Figs. 12(b - e). A strong effect of the increased
889 resolution is observed below 500 m, reducing the negative bias by 70% near the surface. Above 500 m,
890 the effects of higher resolution are limited, with an MBE reduction of 12% in the 0.6 – 2 km. Although
891 the near-surface NO₂ concentrations at 1.4° resolution are overestimated, the values are within the
892 standard deviation of the observations. At around 200m, winter mean NO₂ concentrations at 1.4°

893 resolution are identical to the observations (~9 ppbv), and the summer mean is overestimated. Moreover,
894 the NO₂ levels above 2 km are similar at both resolutions. The resolution effects on NO₂ profiles vary
895 with the location and season (Williams et al., 2017). For example, CHASER NO₂ at 1.1° resolution
896 improved the agreement with aircraft observations below 650 hPa significantly over the Denver
897 metropolitan area (Sekiya et al. 2018), whereas, at Chiba, the 1.4° resolution improved the surface
898 estimates. Consequently, the horizontal resolution is not the only reason for the model underestimation.
899 Other factors such as the vertical resolution, uncertainties in emission inventories, and chemical kinetics,
900 can also affect the simulated NO₂ estimates. Effects of the emission inventory is discussed in section
901 3.3.4.

902 Figure 12(f) shows the smoothed NO₂ profiles at both resolutions. Although the profile shapes are
903 different, the smoothed profiles are almost identical, which demonstrates that, smoothed NO₂ profile
904 sensitivity to a priori choice is mostly independent of the model resolution.

905

906 **Table 8:** Comparison of the seasonal mean NO₂ profiles (0-2 km) among MAX-DOAS and CHASER simulations
907 at 2.8° and 1.4° resolutions at Chiba. MBE at (CHASER – MAX-DOAS) 1.4° and 2.8° are the mean bias error at
908 the respective resolutions. The MBE unit is ppbv.

| Season | MBE at 1.4° | MBE at 2.8° |
|---------|-------------|-------------|
| Overall | -2.24 | -3.37 |
| Spring | -2.26 | -3.23 |
| Summer | -1.50 | -2.47 |
| Autumn | -1.57 | -2.57 |
| Winter | -3.44 | -5.07 |

909

910

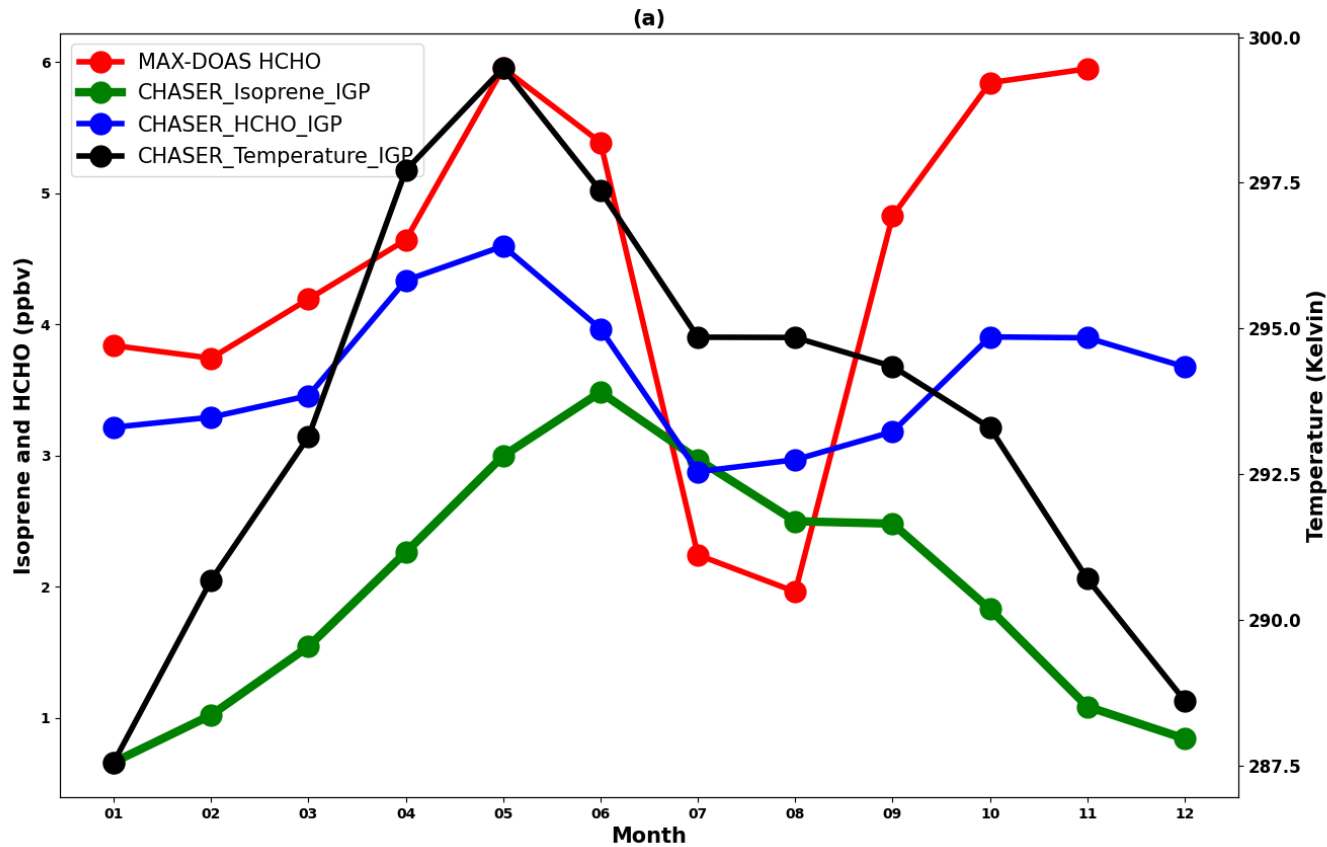
911

912

913

914 **3.3.3 Evaluation of CHASER HCHO in the IGP region**

915 The IGP is the most fertile region in South Asia, which accounts for approximately 50% of the total
916 agricultural production of India and is one of the significant contributing regions to the global greening
917 based on leaf area index (Sarmah et al., 2021). Moreover, IGP is one of the regional HCHO hotspots in
918 India (Chutia et al., 2019). The observed HCHO seasonality at Pantnagar is consistent with that reported
919 by Mahajan et al. (2015) for the entire IGP region. Consequently, comparison with the HCHO retrievals
920 in Pantnagar can assess the model capability in the IGP region. The spatial representiveness is a
921 limitation for comparison between a point measurement and regional simulations. Thus, the results are
922 interpreted qualitatively. Because of the availability of a dataset with continuous observations, only the
923 comparison for 2017 is shown in Fig. 13.



924

925 **Figure 13.** Seasonal variations in the MAX-DOAS (red) and CHASER (blue) HCHO concentrations at Pantnagar
926 and the IGP region, respectively, in 2017. The coincident dates between the observations and model are plotted

only. The CHASER simulated isoprene and temperature seasonality are shown respectively, in green and black colours. Only the daytime simulated values were considered for the plot.

The modeled HCHO seasonal variations in the IGP region correlate well with the observations at Pantnagar ($R \sim 0.80$). The enhancement in the HCHO concentrations during the spring and post-monsoon season is well reproduced by CHASER, which indicates that CHASER can capture HCHO variation in complex terrain region such as IGP. Figure 13 also depicts the isoprene concentrations and temperature in the IGP region, in addition to the HCHO concentrations. Oxidization of precursor hydrocarbons and photochemical reactions are the most dominant sources of HCHO. Also, isoprene is the most abundant hydrocarbon in the atmosphere. The average ambient isoprene concentrations during July, August, and September in the IGP region are 1.4 ± 0.3 ppbv (Mishra et al., 2020). Therefore, the CHASER isoprene concentration range of $1.5 - 2$ ppbv during the monsoon season seems reasonable. The HCHO concentrations in the IGP region reach a peak during the spring and post-monsoon seasons. A strong correlation between HCHO, isoprene, and temperature variation ($R \sim 0.90$) during the first half of the year indicates that the change in biogenic emissions strongly drives the HCHO seasonal modulation. The observed enhancement in the HCHO levels during spring at Pantnagar is related to biomass burning. The biomass burning events are primarily concentrated in the northwest IGP region (Kumar and Sinha, 2021), where the site is located. On a regional scale, the biomass burning effects is expected to smear. Thus, the strong effect of the biogenic emission on the regional HCHO modulation is reasonable. HCHO modulation differs from isoprene and temperature during the post-monsoon period, suggesting a greater role of biomass burning and anthropogenic emissions. Consequently, the physical processes driving the HCHO seasonality in the IGP region are well reflected in the CHASER simulations.

3.3.4 Effects of the model resolution and emission inventories on results

Effects of the spatial resolution on the evaluation results is assessed by comparing the results of CHASER simulations at 2.8° and 1.4° resolutions with the surface observations, as shown in Fig. 14. Only, the simulated surface HCHO and NO_2 concentrations during 2017 are shown only. The statistics are provided in Table 9. For the Pantnagar site, only the simulations are presented. At Phimai, the HCHO simulations

differ by 3%. The standard simulation shows better agreement with the observations. The higher MBE at 1.4° occurred mostly because of the model overestimation during the wet season. The NO₂ mixing ratios at the two resolution differ by 9%. The MBEs for both trace gases at Phimai are less than 1 ppbv. Thus, the HCHO and NO₂ standard simulations at 2.8° can be regarded as reasonable for regions characterized by low NO₂ levels (<1 ppbv). At Chiba, surface NO₂ and HCHO mixing ratios at 1.4° resolution differ respectively, by 61 and 19%. The NO₂ MBE at 1.4° resolution improved significantly, indicating a strong effect of the model resolution. However, discussion in section 3.2.2 showed limited resolution-based improvement in the overall profile. Results for MBE in the HCHO mixing ratios at 1.4° mostly improved during summer. The wintertime HCHO estimates at both resolutions are similar. In contrast to Chiba and Phimai, differences in the HCHO simulations (30%) at Pantnagar are greater than those of NO₂ (3%). The effect of model resolution varying with location and season was also reported by Sekiya et al. (2018). Compared to the other two sites, differences in the NO₂ simulations at Chiba are larger. This finding is consistent with the results by William et al (2017), which found larger differences with changing model resolution over urban areas.

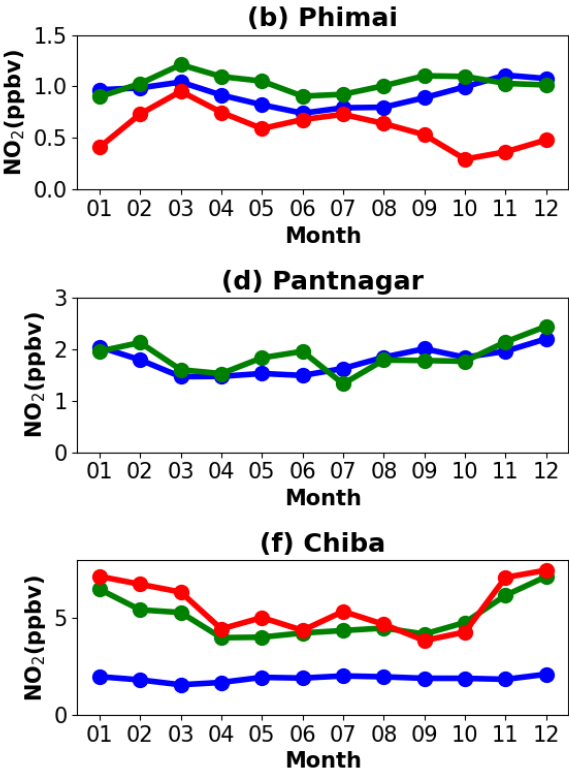
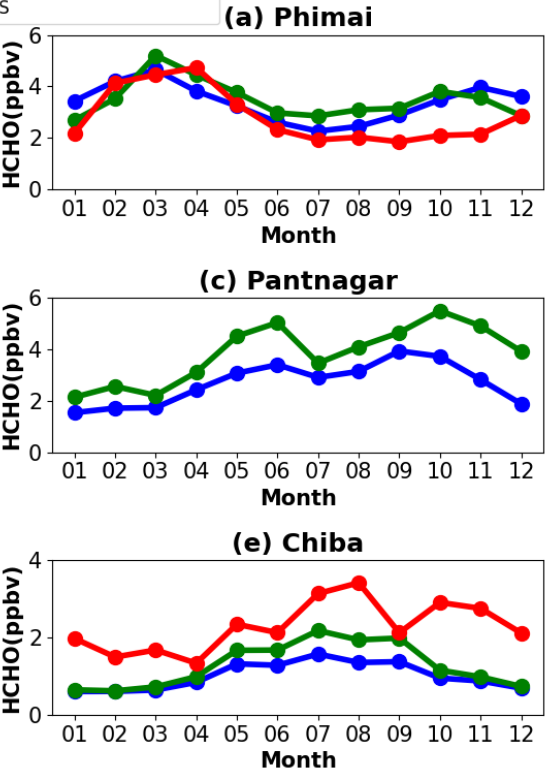
Although the NO_x estimates for the low NO₂ regions seem reasonable, global NO_x emissions have changed since 2008(i.e., EDGAR-HTAP (2008) emissions used for this study). A recent study by Miyazaki et al. (2020) reported changes in global NO_x emissions from 2005 to 2018. They found a continuous 30% increase in NO_x emissions in India since 2005. REAS v3 (Regional Emission inventory in Asia version 3) inventory estimated a 23% increase in NO_x emissions in India between 2010 - 2015, and power plants were the most significant contributor. Many power plants are clustered along the IGP region (Nair et al., 2007). Thus, the current simulation settings are likely to underestimate the NO₂ mixing ratios and columns in the IGP region. Figure S8 presents comparison of CHASER and OMI NO₂ columns for 2017 over the IGP region. Although the modeled columns are biased by 32% in the lower side, the spatial correlation between the datasets is high ($r=0.78$). CHASER values lie within the range of variation of the observations. Although underestimated, NO₂ estimates in the IGP based on the current inventory are yet reasonable. Sekiya et al., (2018) used higher model resolution and updated emission inventory (HTAP 2010 for simulations in 2014) and reported ~30% lower MBE over India. However, the RMSE values of both studies are comparable.

983 NO_x emissions in Japan have shown continuous decline since the execution of pollution control policies
984 in 1970 (Ohara et al., 2020). Irie et al. (2021) reported a declining trend in NO₂ levels in Chiba since
985 2012, echoing results obtained by Miyazaki et al. (2020) throughout Japan. The bias between CHASER
986 and OMI NO₂ column over Japan is non-significant (Fig. S8 and Table S3). Thus, an updated inventory
987 will not substantially affect the comparison results at the Chiba site. NO_x emissions increased
988 considerably in Southeast Asia. CHASER NO₂ estimates for Thailand based on HTAP 2008 inventory
989 are biased by 45% in the lower side compared to OMI (Fig. S8). However, Phimai being a rural site, the
990 NO_x levels are expected to be low. Changes in biomass burning NO_x estimates are likely to affect the
991 model estimates. Because, the NO₂ levels at Phimai are mostly less than 1 ppbv, the effect of updated
992 inventory on the comparison results is expected to be minimal.

993 CHASER HCHO columns over Japan, the IGP region, and Thailand are negatively biased respectively,
994 by 60, 36, and 32% compared to OMI observations, with *r*-values of 0.5 – 0.7 (Fig. S8). Surl et al. (2018)
995 reported spatial correlation of ~0.5 between GEOS-CHEM and OMI over the IGP region. Anthropogenic
996 VOC emissions in India and other Asian cities have increased since 2005, whereas a negative trend has
997 been observed over Japan (Bauwens et al., 2022). The REAS inventory estimated a 5% increase in
998 NMVOCs in India since 2005. Moreover, anthropogenic emission contributes strongly to the HCHO
999 abundances in the IGP region (Kumar and Sinha 2021). Thus, updated anthropogenic VOC emission
1000 inventory is likely to improve the model HCHO estimates in the study regions. However, the formation
1001 pathway of HCHO from isoprene emissions is a non-linear function of NO_x chemistry. Consequently, the
1002 effects of NO_x emissions changes on the overall HCHO simulations cannot be assessed based on current
1003 analyses explained herein.

1004

CHASER simulations at 2.8 degree
 CHASER simulations at 1.4 degree
 MAX-DOAS



1005
 1006
 1007
 1008
 1009
 1010
 1011
 1012
 1013
 1014
 1015
 1016
 1017

Figure 14. Seasonal variation in the surface HCHO and NO₂ mixing ratios at (a & b) Phimai, (c & d) Pantnagar, and (e & f) Chiba simulated at spatial resolutions of 2.8° × 2.8° (blue) and 1.4° × 1.4° (green). Coincident MAX-DOAS NO₂ and HCHO VMRs in the 0-1 km layer at Phimai and Chiba are plotted in red. Observation at Pantnagar are discarded. Only the datasets for 2017 are plotted.

1018
1019
1020
1021
1022
1023
1024
1025
1026
1027
1028
1029
1030
1031
1032
1033
1034
1035
1036
1037
1038

Table 9: The comparison between the observations and simulations at 2.8° and 1.4° spatial resolutions. The MBE is the mean bias error. The unit of MBE is ppbv.

| Site | Trace gas | MBE at 2.8° | MBE at 1.4° | Differences between the simulations |
|-----------|-----------------|-------------|-------------|-------------------------------------|
| Phimai | HCHO | 0.54 | 0.65 | 3% |
| Phimai | NO ₂ | 0.33 | 0.43 | 9% |
| Chiba | HCHO | -1.27 | -1.00 | 19% |
| Chiba | NO ₂ | -0.52 | -3.69 | 61% |
| Pantnagar | | | | 30% |
| Pantnagar | | | | 3% |

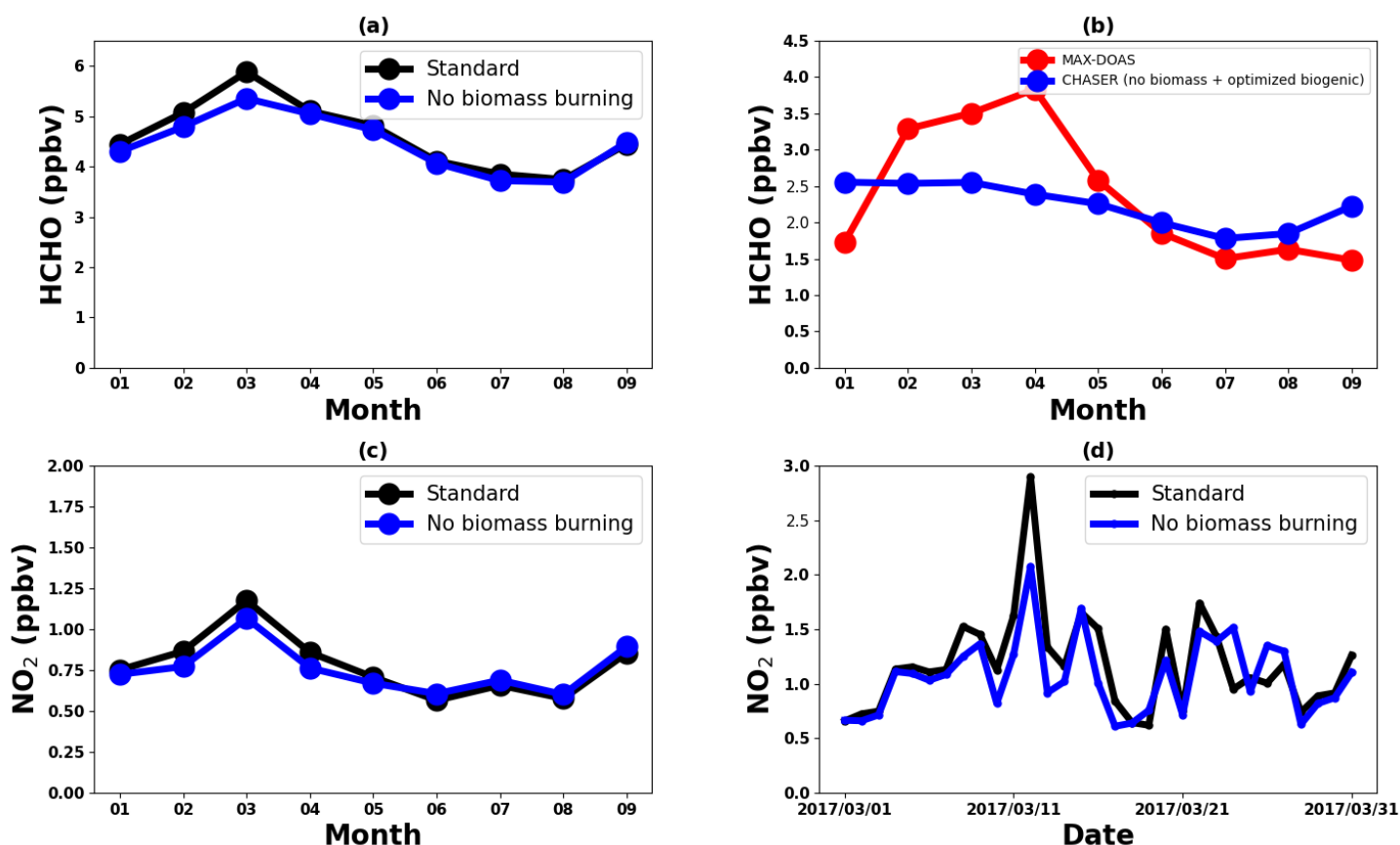
3.4 Contribution estimates

3.4.1 Contribution from biomass burning to the HCHO and NO₂ abundances at Phimai

Good agreement between the datasets in the 0 - 1 km layer at Phimai can quantify biomass burning contributions to the HCHO and NO₂ concentrations. Figure 15 presents results of simulations L1_HCHO, L1_opt, and L1_NO₂. The simulation settings are presented in Table 3. For better readability, the switched-off emissions criterion is described in the legends of Fig.15. The plots present mean mixing ratios in the 0 – 1 km layer. Biomass burning contributes ~10% to the HCHO concentrations at Phimai during the dry season. However, based on the observations, a greater effect of biomass burning is expected. During the wet season, the MAX-DOAS and CHASER HCHO surface mixing ratios are, respectively, ~2 and ~4 ppbv (Fig. 10), indicating overestimation of the biogenic emissions in CHASER. Figure 15(b) shows the HCHO concentration obtained from simulation L1_opt and MAX-DOAS

1039 observations in 2017. In the L1_opt simulation setting, the biomass burning emissions are switched off;
 1040 the biogenic emissions are optimized to reproduce results analogous to those obtained from observations
 1041 during the wet season. In the absence of biomass burning, the surface HCHO concentrations at Phimai
 1042 would be ~2 ppbv, indicating a biomass burning contribution of ~20–50% during the dry season. The
 1043 observed interseason difference in the HCHO concentration at Phimai is ~60%. Consequently, the revised
 1044 biomass burning contribution estimate is more reasonable. Pyrogenic emissions contributions to the NO₂
 1045 concentrations at Phimai are ~10% during the dry season (Fig. 15(c)). Because the NO₂ concentrations
 1046 are low at Phimai, the simulation results obtained for March, when the influence of biomass burning is
 1047 highest, are used to derive a better contribution estimate. In the absence of biomass burning, the NO₂
 1048 concentration during March would be about 0.84 ppbv (Fig.15(d)), indicating a contribution as high as
 1049 35% to the NO₂ concentrations at Phimai.

1050



1051

1052 **Figure 15.** (top panel) (a) Seasonal variations in the HCHO concentrations in the 0 - 1 km layer at Phimai, as
1053 obtained from the standard and L1_HCHO simulations. Pyrogenic emissions of VOCs are switched off in
1054 L1_HCHO. (b) The HCHO seasonal variation in Phimai in 2017, as obtained from the MAX-DOAS observations
1055 (red) and L1_opt simulations. The pyrogenic VOC emissions were switched off, and the biogenic emissions were
1056 reduced by 50% in L1_opt. The coincident dates between the observation and the simulations are shown only.
1057 (bottom panel) (c) Seasonal variations in the NO₂ surface concentrations at Phimai in 2017, as obtained from the
1058 standard and L1_NO₂ simulations. (d) Standard and L1_NO₂ simulation outputs of the daily mean NO₂ surface
1059 concentrations during March 2017. The pyrogenic NO₂ emissions were switched off in the L1_NO₂ simulation.
1060 Only the daytime values from 09:00 – 15:00 LT are used to calculate the seasonal mean.

1061

1062

1063 **3.4.2 Contribution of soil NO_x emissions at Phimai**

1064 Because soil NO_x emissions are included in CHASER simulations, the NO₂ contributions from soil
1065 emissions are quantified. Figure 16 presents the monthly mean surface NO₂ concentrations at Phimai in
1066 2017, simulated including (standard) and switching off (L1_NO₂) the soil NO_x emissions. The NO₂
1067 concentrations between 09 and 12 hr. were used to calculate the monthly mean concentrations. Soil
1068 emissions contribute ~20% of the overall NO₂ concentrations at Phimai, with higher contributions during
1069 the wet season. The highest soil contribution of about 25% occurs in July.

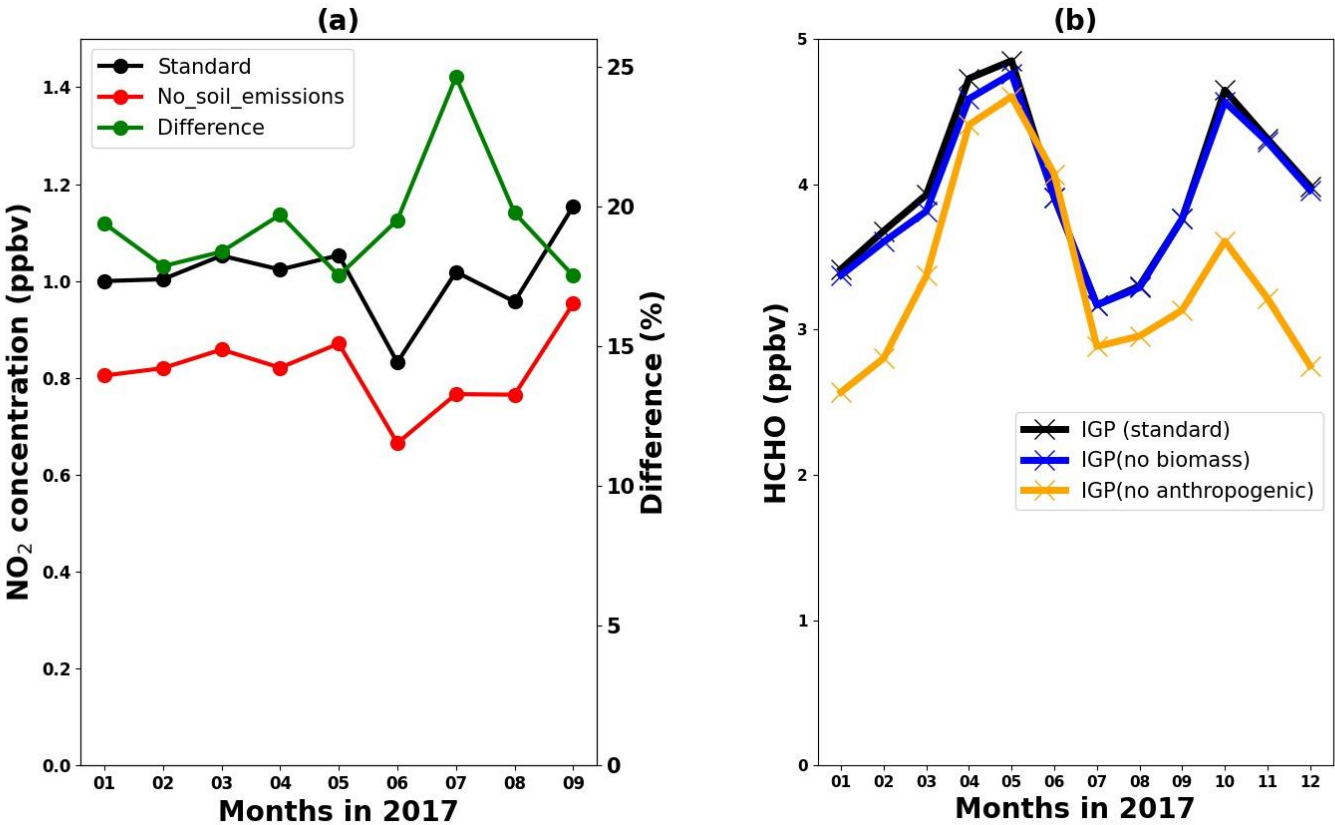
1070

1071 **3.4.3 Contribution from pyrogenic and anthropogenic emissions to the HCHO abundances in the** 1072 **IGP region**

1073 Figure 16(b) presents the standard, L1_HCHO (pyrogenic VOC emissions switched off), and L2
1074 (anthropogenic VOC emissions switched off) HCHO simulations in the IGP region. According to
1075 L1_HCHO simulation results, effects of biomass burning emissions on the regional HCHO modulation
1076 are small (~12%). The HCHO concentrations in India have biogenic, anthropogenic, and pyrogenic VOC
1077 sources. However, biogenic VOCs are the primary driver of the over HCHO variation (Surl et al., 2018).
1078 Consequently, two reasons might be responsible for the small effects of pyrogenic emissions on HCHO
1079 concentrations: (1) Overestimation of the biogenic emission or underestimation of pyrogenic emissions

1080 in the model. (2) Stronger effects of anthropogenic VOC emissions than of pyrogenic VOCs. The L2
 1081 simulations show that anthropogenic emissions contribute up to 30% of the HCHO concentration in the
 1082 IGP region, with a maximum contributed during the post-monsoon season, which coincides with the
 1083 lower isoprene concentration (i.e., biogenic emissions) and temperature (Fig. 14). Moreover, Kumar and
 1084 Sinha (2021) reported high acetaldehyde concentrations from anthropogenic emissions in the IGP region
 1085 throughout the year. Consequently, anthropogenic emissions are likely to be a significant driver of HCHO
 1086 concentrations in the IGP region after biogenic emissions.

1087
 1088



1089
 1090 **Figure 16.** (a) Monthly mean NO_2 concentrations at Phimai were estimated from the standard (black) and L1_ NO_2
 1091 (red) simulations. The soil NO_x emissions are switched off in the LI_ NO_2 simulation. The green line represents the
 1092 percentage difference between the two simulations. (b) Seasonal variations in the HCHO concentrations in the IGP

1093 region, obtained from the standard, L1_HCHO (pyrogenic VOC emission switched off), and L2 simulations
1094 (anthropogenic VOC emissions switched off). The simulations for 2017 are shown and analysed. Daytime values
1095 from 09:00-12:00 and 09:00 – 15:00 LT were selected respectively, for Phimai and IGP.

1096

1097 **4 Conclusions**

1098 Using the JM2 algorithm, NO₂ and HCHO concentrations and profiles were retrieved from MAX-DOAS
1099 observations at three A-SKY sites during January 2017 - December 2018. The retrieved products were
1100 used to evaluate the global chemistry transport model CHASER simulations at the three sites. At all three
1101 locations, the seasonal variation of both trace gases was consistent throughout the investigated period. At
1102 Phimai and Pantnagar, biomass burning led to enhanced HCHO and NO₂ concentrations, respectively,
1103 during the dry season and spring and post-monsoon season. At Chiba, the HCHO variation was consistent
1104 with the temperature-led seasonal changes in biogenic emissions. The changes in the dry season HCHO
1105 and NO₂ levels at Phimai during 2015 - 2018 were consistent with the number of fire events.

1106 The R_{FN} values were biased towards a particular regime when the standard transition range $1 < R_{FN} < 2$
1107 (Duncan et al., 2010) was used. The parameterization of Souri et al. (2020) provides a better estimate of
1108 the transition region. The classification results of the revised transition region at Phimai and Pantnagar
1109 contradicted the results based on the standard transition range. However, they were more reasonable. Such
1110 a method based on observations, is therefore influenced by measurement constraints. More observational
1111 evidence must be accumulated to standardize this method. Overall, the results further indicated that that
1112 the standard transition region is not valid globally.

1113 Despite the use of an old NO_x emission inventory the simulated NO₂ and HCHO spatial distributions
1114 agreed reasonably well with those observed from satellite- observations. The modeled regional NO₂
1115 columns estimates were within the 2-sigma variability range of OMI NO₂ retrievals. Although the
1116 negative bias in HCHO comparison was higher than that of NO₂, the model demonstrated good
1117 capabilities for simulating the HCHO seasonal variation in different regions.

1118 CHASER showed good capabilities at Phimai, characterized as a VOC-rich and low NO₂ (<1 ppbv)
1119 region. In both seasons, the observed and modeled profiles (HCHO and NO₂) agreed within the one sigma

1120 standard deviation of the measurements, despite general overestimation of the model. Furthermore, both
1121 wet season HCHO profiles were almost identical in the 0.5 – 4 km layer in both datasets.
1122 CHASER demonstrated limited performances at Chiba.NO₂ at higher resolution (i.e.,1.4°) mainly
1123 improved the surface estimates, reducing the overall MBE in the 0 - 2 km layer by 35%. Finer resolution
1124 would improve the HCHO estimates in Chiba by 10%; however, it has yet to be underestimated.
1125 Sensitivity studies for the Phimai site estimated biomass burning contributions to the respective HCHO
1126 and NO₂ concentrations up to ~50 and ~ 35%, respectively. On average, 20% of the NO₂ level originates
1127 from soil NO_x emissions, which increased to 25% in July. Anthropogenic emissions (contribution up to
1128 30%) have a more strongly affect VOC variation in the IGP region than biomass burning, which is
1129 consistent with reports presented in the literature.

1130

1131

1132 *Code availability.* The CHASER and JM2 source codes are not available publicly. Dr. Kengo Sudo
1133 (kengo@nagoya-u.jp) is the contact person for readers and researchers interested in the CHASER model.
1134 In addition, Dr. Hitoshi Irie (hitoshi.irie@chiba-u.jp) will answer queries related to the JM2 codes.

1135

1136 *Data availability:* The MAX-DOAS data used in the study are publicly accessible on the A-SKY network
1137 website (<http://atmos3.cr.chiba-u.jp/a-sky/data.html>). Upon request, the corresponding author can
1138 provide the CHASER simulations and MAX-DOAS averaging kernel data.

1139

1140 *Author contributions:* HMSH conceptualized the study, conducted the model simulations, analysed the
1141 observational and simulation data, and drafted the manuscript. AMF helped with the data processing. HI
1142 developed the JM2 code and maintained the A-SKY network. KS developed the CHASER model and
1143 supervised the study. MN is the PI of the Pantnagar site. AD and MN shared their experience to explain
1144 the results. HI, KS, AD, MN, and AMF commented and provided feedback on the final results and
1145 manuscript.

1146

1147 *Conflict of Interest:* The authors declare that they have no conflict of Interest

1148

1149 *Acknowledgments:* This research is supported by the Global Environmental Research fund (S-12 and S-
1150 20) of the Ministry of the Environment (MOE), Japan, and JSPS KAKENHI Grants: JP20H04320,
1151 JP19HO5669, and JP19H04235. The CHASER model simulations are partly performed with the
1152 supercomputer (NEC SX-Aurora TSUBASA) at the National Institute for environmental studies (NIES),
1153 Tsukuba, Japan. The authors are grateful to the OMI and TROPOMI data providers. Support from ISRO-
1154 ATCTM project for Pantnagar site is also acknowledged.

1155

1156

1157

1158 **References**

1159 Amnuaylojaroen, T., Inkom, J., Janta, R., & Surapipith, V. : Long range transport of southeast asian pm_{2.5}
1160 pollution to northern Thailand during high biomass burning episodes. *Sustainability*, 12(23), 10049. doi:
1161 <https://doi.org/10.3390/su122310049>, 2020

1162

1163 Arlander, D., Brüning, D., Schmidt, U., and Ehhalt, D. : The tropospheric distribution of formaldehyde during
1164 TROPOZ II, *J. Atmos. Chem.*, 22(3), 251-269, <https://doi.org/10.1007/BF00696637>, 1995

1165

1166 Bauwens, M, Verreyken, B, Stavrou, T, Müller, JF, & De Smedt, I. : Spaceborne evidence for
1167 significant anthropogenic VOC trends in Asian cities over 2005–2019. *Environ. Res. Lett.*, 17(1),
1168 015008. doi:<https://iopscience.iop.org/article/10.1088/1748-9326/ac46eb/>, 2022

1169

1170

1171 Biswas, M. S., Ghude, S. D., Gurnale, D., Prabhakaran, T., and Mahajan, A. S. : Simultaneous Observations of
1172 Nitrogen Dioxide, Formaldehyde and Ozone in the Indo-Gangetic Plain. *Aerosol Air Qual. Res.*, 19(8),
1173 1749-1764, <https://doi.org/10.4209/aaqr.2018.12.0484>, 2019

1174

1175 Biswas, M. S., & Mahajan, A. S. : Year-long Concurrent MAX-DOAS Observations of Nitrogen Dioxide and
1176 Formaldehyde at Pune: Understanding Diurnal and Seasonal Variation Drivers. *Aerosol Air Qual. Res.*,
1177 21(6), 200524. doi:<https://doi.org/10.4209/aaqr.200524>, 2021

1178

1179

1180

1181 Boeke, N. L., Marshall, J. D., Alvarez, S., Chance, K. V., Fried, A., Kurosu, T. P., Rappengluck, B., Richter,
1182 D., Walega, J., & Weibring, P. : Formaldehyde columns from the Ozone Monitoring Instrument: Urban
1183 versus background levels and evaluation using aircraft data and a global model. J. Geophys. Res., 116(D5).
1184 2011

1185

1186

1187

1188 Bond, D. W., Zhang, R., Tie, X., Brasseur, G., Huffman, G., Orville, R. E., and Boccippio, D. J. : NO_x production
1189 by lightning over the continental United States, J. Geophys. Res., 106(D21), 27701-27710,
1190 <https://doi.org/10.1029/2000JD000191>, 2001

1191

1192 Bogumil, K., J. Orphal, T. Homann, S. Voigt, P. Spietz, O. Fleischmann, A. Vogel, M. Hartmann, H. Kromminga,
1193 and H. Bovensmann : Measurements of molecular absorption spectra with the SCIAMACHY pre-flight
1194 model: instrument characterization and reference data for atmospheric remote-sensing in the 230–2380 nm
1195 region, J. Photochem. Photobiol. A, 157(2), 167-184, doi:10.1016/S1010-6030(03)00062-5, 2003

1196

1197

1198

1199

1200

1201 Burkert, J., Andrés-Hernández, M. D., Stöbener, D., Burrows, J. P., Weissenmayer, M., & Kraus, A. (2001) :
1202 Peroxy radical and related trace gas measurements in the boundary layer above the Atlantic Ocean, J.
1203 Geophys. Res., 106(D6), 5457-5477, <https://doi.org/10.1029/2000JD900613>, 2001

1204

1205

1206

1207 Cárdenas, L., Rondón, A., Johansson, C., & Sanhueza, E. : Effects of soil moisture, temperature, and inorganic
1208 nitrogen on nitric oxide emissions from acidic tropical savannah soils. J. Geophys. Res., 98(D8), 14783-
1209 14790, <https://doi.org/10.1029/93JD01020>, 1993

1210

1211 Chaliyakunnel, S., Millet, D. B., and Chen, X. : Constraining emissions of volatile organic compounds over the
 1212 Indian subcontinent using space-based formaldehyde measurements. *J. Geophys. Res.*, 124(19), 10525-
 1213 10545, <https://doi.org/10.1029/2019JD031262>, 2019
 1214
 1215
 1216 Chance, K. V., and R. J. D. Spurr. : Ring effect studies: Rayleigh scattering, including molecular
 1217 parameters for rotational Raman scattering: and the Fraunhofer spectrum, *Appl. Opt.* , 36(21),
 1218 5224-5230 doi:10.1364/AO.36.005224,1997
 1219
 1220 Chutia, L., Ojha, N., Girach, I. A., Sahu, L. K., Alvarado, L. M. A., Burrows, J. P., Pathak., P., & Bhuyan, P. K. :
 1221 Distribution of volatile organic compounds over Indian subcontinent during winter: WRF-chem simulation
 1222 versus observations. *Environ. Pollut.*, 252, 256-269. doi:<https://doi.org/10.1016/j.envpol.2019.05.097>,
 1223 2019
 1224
 1225
 1226
 1227 Clémer, K., Van Roozendaal, M., Fayt, C., Hendrick, F., Hermans, C., Pinardi, G., Spurr, R., Wang, P., and De
 1228 Mazière, M. : Multiple wavelength retrieval of tropospheric aerosol optical properties from MAXDOAS
 1229 measurements in Beijing, *Atmos. Meas. Tech.*, 3(4), 863-878, <https://doi.org/10.5194/amt-3-863-2010>,
 1230 2010
 1231
 1232
 1233 Colella, P., & Woodward, P. R. : The piecewise parabolic method (PPM) for gas-dynamical simulations. *J. Comput.*
 1234 *Phys.*, 54(1), 174-201, [https://doi.org/10.1016/0021-9991\(84\)90143-8](https://doi.org/10.1016/0021-9991(84)90143-8), 1984
 1235
 1236
 1237
 1238
 1239 Crutzen, P. J. : The influence of nitrogen oxides on the atmospheric ozone content. *Q. J. Roy. Meteor. Soc.*, 96(408),
 1240 320-325, <https://doi.org/10.1002/qj.49709640815>, 1970
 1241
 1242

Davidson, E. A., Vitousek, P. M., Matson, P. A., Riley, R., García-Méndez, G., & Maass, J. M. : Soil emissions of
 nitric oxide in a seasonally dry tropical forest of Mexico. *J. Geophys. Res.*, 96(D8), 15439-15445,
<https://doi.org/10.1029/91JD01476>, 1991

De Smedt, I. , Pinardi, G., Vigouroux, C., Compernelle, S., Bais, A., Benavent, N., Eichmann, K-U., Hedelt, P.,
 Hendricks, F., Irie, H., Kumar, V., Lambert, J-C., Langerock, B., Lerot, C., Liu, C., Loyola, D., Pitters, A.,
 Richter, A., Cardens, C.R., Romahn, F., Ryan, R.G., Sinha, V., Theys, N., Vlietinck, J., Waggoner, T., Wang,
 T., YU, H., and Van Roozendaal, M.,: Comparative assessment of TROPOMI and OMI formaldehyde
 observations and validation against MAX-DOAS network column measurements. *Atmos. Chem. Phys.*,
 21(16), 12561-12593. doi:<https://doi.org/10.5194/acp-21-12561-2021>, 2021

Duncan, B. N., Yoshida, Y., Damon, M. R., Douglass, A. R., and Witte, J. C. : Temperature dependence of factors
 controlling isoprene emissions. *Geophys. Res. Lett.*, 36(5), <https://doi.org/10.1029/2008GL037090>, 2009

Emori, S., Nozawa, T., Numaguti, A., & Uno, I. : Importance of cumulus parameterization for precipitation
 simulation over East Asia in June. *J. Meteorol. Soc. Jpn.*, 79(4), 939-947.
<https://doi.org/10.2151/jmsj.79.939>, 2001

Fleischmann, O. C., M. Hartmann, J. P. Burrows, and J. Orphal : New ultraviolet absorption cross-sections of BrO
 at atmospheric temperatures measured by time-windowing Fourier transform spectroscopy, *J. Photocho.*
Photobio. A, 168(1), 117-132, doi:10.1016/j.jphotochem.2004.03.026, 2004

1275 Franco, B., Hendrick, F., Van Roozendaal, M., Müller, J.-F., Stavrakou, T., Marais, E. A., Bovy, B., Bader, W.,
 1276 Fayt, C., Hermans, C., Lejuene, B., Pinardi, G., Sevais, C., and Mahieu, E. : Retrievals of formaldehyde
 1277 from ground-based FTIR and MAX-DOAS observations at the Jungfraujoch station and comparisons with
 1278 GEOS-Chem and IMAGES model simulations. *Atmos. Meas. Tech.*, 8(4), 1733-1756,
 1279 <https://doi.org/10.5194/amt-8-1733-2015>, 2015
 1280
 1281 Fu, T. M., Jacob, D. J., Wittrock, F., Burrows, J. P., Vrekoussis, M., and Henze, D. K. : Global budgets of
 1282 atmospheric glyoxal and methylglyoxal, and implications for formation of secondary organic aerosols, *J.*
 1283 *Geophys. Res.*, 113(D15), <https://doi.org/10.1029/2007JD009505>, 2008
 1284
 1285
 1286 Frieß, U., Monks, P. S., Remedios, J. J., Rozanov, A., Sinreich, R., Wagner, T., & Platt, U. : MAX-DOAS O4
 1287 measurements: A new technique to derive information on atmospheric aerosols: 2. Modeling studies. *J.*
 1288 *Geophys. Res.*, 111(D14), <https://doi.org/10.1029/2005JD006618>, 2006
 1289
 1290 Frieß, U., Klein Baltink, H., Beirle, S., Clémer, K., Hendrick, F., Henzing, B., Irie, H., de Leeuw, G., Li, A.,
 1291 Moerman, M. M., van Roozendaal, M., Shaiganfar, R., Wagner, T., Wang, Y., Xie, P., Yilmaz, S., and
 1292 Zieger, P. : Intercomparison of aerosol extinction profiles retrieved from MAX-DOAS measurements.
 1293 *Atmos. Meas. Tech.*, 9(7), 3205-3222, <https://doi.org/10.5194/amt-9-3205-2016>, 2016
 1294
 1295 Fukushima, A., Kanamori, H., & Matsumoto, J. : Regionality of long-term trends and interannual variation of
 1296 seasonal precipitation over India. *Prog Earth Planet Sci*, 6(1), 1-20. doi:[https://doi.org/10.1186/s40645-](https://doi.org/10.1186/s40645-019-0255-4)
 1297 019-0255-4, 2019
 1298
 1299
 1300 Hak, C., Pundt, I., Trick, S., Kern, C., Platt, U., Dommen, J., Ordóñez, C., Prévôt, A. S. H., Junkermann, W.,
 1301 Astorga-Lloréns, C., Larsen, B. R., Mellqvist, J., Strandberg, A., Yu, Y., Galle, B., Kleffmann, J., Lörzer,
 1302 J. C., Braathen, G. O., and Volkamer, R. : Intercomparison of four different in-situ techniques for ambient
 1303 formaldehyde measurements in urban air, *Atmos. Chem. Phys.*, 5(11), 2881-2900.
 1304 <https://doi.org/10.5194/acp-5-2881-2005>, 2005
 1305
 1306

1307

1308 Hall, S. J., Matson, P. A., and Roth, P. M. : NO_x emissions from soil: implications for air quality modeling in
1309 agricultural regions. *Annu. Rev. Energy Environ.*, 21(1), 311-346.
1310 <https://doi.org/10.1146/annurev.energy.21.1.311>, 1996

1311

1312

1313 Halla, J. D., Wagner, T., Beirle, S., Brook, J. R., Hayden, K. L., O'Brien, J. M., Ng, A., Majonis, D., Wenig, M.
1314 O., and McLaren, R : Determination of tropospheric vertical columns of NO₂ and aerosol optical
1315 properties in a rural setting using MAX-DOAS. *Atmos. Chem. Phys.*, 11(23), 12475-12498,
1316 <https://doi.org/10.5194/acp-11-12475-2011>, 2011

1317

1318

1319 Hendrick, F., Müller, J.-F., Clémer, K., Wang, P., De Mazière, M., Fayt, C., Gielen, C., Hermans, C., Ma, J. Z.,
1320 Pinardi, G., Stavrou, T., Vlemmix, T., and Van Roozendaal, M.: Four years of ground-based MAX-
1321 DOAS observations of HONO and NO₂ in the Beijing area, *Atmos. Chem. Phys.*, 14(2), 765-781,
1322 <https://doi.org/10.5194/acp-14-765-2014>, 2014

1323

1324

1325 Hermans, C., A. Vandaele, S. Fally, M. Carleer, R. Colin, B. Coquart, A. Jenouvrier, and M.-F. Merienne.
1326 : Absorption cross-section of the collision-induced bands of oxygen from the UV to the NIR, in *Weakly*
1327 *interacting molecular pairs: unconventional absorbers of radiation in the atmosphere*, edited, pp. 193-
1328 202, Springer, 2003.

1329

1330

1331

1332 Hönninger, G., Friedeburg, C. v., and Platt, U. : Multi axis differential optical absorption spectroscopy (MAX-
1333 DOAS), *Atmos. Chem. Phys.*, 4(1), 231-254, <https://doi.org/10.5194/acp-4-231-2004>, 2004

1334

1335 Hoque, H.M. S., Irie, H., and Damiani, A. (2018). First MAX-DOAS Observations of Formaldehyde and Glyoxal
1336 in Phimai, Thailand. *J. Geophys. Res.*, 123(17), 9957-9975, <https://doi.org/10.1029/2018JD028480>, 2018a

1337

1338 Hoque, H. M. S., Irie, H., Damiani, A., Rawat, P., and Naja, M. : First simultaneous observations of formaldehyde
1339 and glyoxal by MAX-DOAS in the Indo-Gangetic Plain region. *Sola.* , [https://doi.org/10.2151/sola.2018-](https://doi.org/10.2151/sola.2018-028)
1340 028, 2018b

1341

1342

1343 Houweling, S., Dentener, F., and Lelieveld, J. : The impact of nonmethane hydrocarbon compounds on tropospheric
1344 photochemistry. *J. Geophys. Res.*, 103(D9), 10673-10696, <https://doi.org/10.1029/97JD03582>, 1998

1345

1346

1347

1348 Huber, D. E., Steiner, A. L., & Kort, E. A. : Daily Cropland Soil NO_x Emissions Identified by TROPOMI and
1349 SMAP. *Geophys. Res. Lett.*, 47(22), e2020GL089949, <https://doi.org/10.1029/2020GL089949>, 2020

1350

1351

1352

1353 Irie, H., Kanaya, Y., Akimoto, H., Iwabuchi, H., Shimizu, A., & Aoki, K. : First retrieval of tropospheric aerosol
1354 profiles using MAX-DOAS and comparison with lidar and sky radiometer measurements. *Atmos. Chem.*
1355 *Phys.*, 8(2), 341-350, <https://doi.org/10.5194/acp-8-341-2008>, 2008a

1356 Irie, H., Kanaya, Y., Akimoto, H., Tanimoto, H., Wang, Z., Gleason, J. F., & Bucsela, E. J. : Validation of OMI
1357 tropospheric NO₂ column data using MAX-DOAS measurements deep inside the North China Plain in
1358 June 2006: Mount Tai Experiment 2006. *Atmos. Chem. Phys.*, 8(22), 6577-
1359 6586, <https://doi.org/10.5194/acp-8-6577-2008>, 2008b.

1360

1361 Irie, H., Kanaya, Y., Akimoto, H., Iwabuchi, H., Shimizu, A., & Aoki, K. : Dual-wavelength aerosol vertical profile
1362 measurements by MAX-DOAS at Tsukuba, Japan. *Atmos. Chem. Phys.*, 9(8), 2741-2749,
1363 <https://doi.org/10.5194/acp-9-2741-2009>, 2009

1364

1365 Irie, H., Takashima, H., Kanaya, Y., Boersma, K., Gast, L., Wittrock, F., Brunner, D., Zhou, Y., Roozendael, M.
1366 V. : Eight-component retrievals from ground-based MAX-DOAS observations. *Atmos. Meas. Tech.*, 4(6),
1367 1027-1044, <https://doi.org/10.5194/amt-4-1027-2011>, 2011

1368

1369 Irie, H., Nakayama, T., Shimizu, A., Yamazaki, A., Nagai, T., Uchiyama, A., Zaizen, Y., Kagamitani, S.,
1370 and Matsumi, Y. : Evaluation of MAX-DOAS aerosol retrievals by coincident observations using CRDS,
1371 lidar, and sky radiometer in Tsukuba, Japan. *Atmos. Meas. Tech.*, 8(7), 2775-2788,
1372 <https://doi.org/10.5194/amt-8-2775-2015>, 2015

1373

1374 Irie, H., Muto, T., Itahashi, S., Kurokawa, J., & Uno, I. : Turnaround of tropospheric nitrogen dioxide pollution
1375 trends in China, Japan, and South Korea. *Sola*, 12, 170-174. doi: <https://doi.org/10.2151/sola.2016-035>,
1376 2016

1377

1378

1379 Irie, H., Yonekawa, D., Damiani, A., Hoque, H.M.S, Sudo, K., & Itahashi, S.; Continuous multi-component MAX-
1380 DOAS observations for the planetary boundary layer ozone variation analysis at Chiba and Tsukuba, Japan,
1381 from 2013 to 2019. *Prog Earth Planet Sci*, 8(1), 1-11. doi:[https://doi.org/10.1186/s40645-021-00424-](https://doi.org/10.1186/s40645-021-00424-9)
1382 9,2021

1383

1384

1385 Ito, A., and Inatomi, M. : Use of a process-based model for assessing the methane budgets of global terrestrial
1386 ecosystems and evaluation of uncertainty. *Biogeosciences*, 9(2), 759-773. [https://doi.org/10.5194/bg-9-](https://doi.org/10.5194/bg-9-759-2012)
1387 759-2012, 2012

1388

1389

1390 Iwabuchi, H. :Efficient Monte Carlo methods for radiative transfer modeling. *J. Atmos. Sci.*, 63(9), 2324-2339,
1391 <https://doi.org/10.1175/JAS3755.1>, 2006

1392

1393

1394 Jang, M., and Kamens, R. M. : Characterization of secondary aerosol from the photooxidation of toluene in the
1395 presence of NO_x and 1-propene, *Environ. Sci. Technol.*, 35(18), 3626-3639.
1396 <https://doi.org/10.1021/es010676+>, 2001

1397

1398

1399 Jin, X., Fiore, A. M., Murray, L. T., Valin, L. C., Lamsal, L. N., Duncan, B., Boersma, K.F., De Smedt, I., Abad,
1400 G.G., Chance, K., and Tonnesen, G. : Evaluating a space-based indicator of surface ozone-NO_x-VOC

sensitivity over midlatitude source regions and application to decadal trends. *J. Geophys. Res.*, 122(19), 10,439-410,461, <https://doi.org/10.1002/2017JD026720>, 2017

Jin, X., & Holloway, T. (2015). Spatial and temporal variability of ozone sensitivity over China observed from the Ozone Monitoring Instrument. *J. Geophys. Res.*, 120(14), 7229-7246. doi: <https://doi.org/10.1002/2015JD023250>

Jenkin, M.E., Young, J.C., & Rickard, A.R. : The MCM v3. 3.1 degradation scheme for isoprene. *Atmos. Chem. Phys.*, 15(20), 11433-11459. doi:<https://doi.org/10.5194/acp-15-11433-2015>, 2015

Joshi, H., Manish, N., Singh, K.P., Kumar, R., Bhardwaj, P., Babu, S.S., Satheesh, S.K., Moorthy, K.K., Chandola, H.C. : Investigations of aerosol black carbon from a semi-urban site in the Indo-Gangetic Plain region, *Atmos. Environ.*, 125, 346-359, <https://doi.org/10.1016/j.atmosenv.2015.04.007>, 2016.

K-1 model developers : K-1 Coupled GCM (MIROC) description, Tech .rep., Center for Climate System Research (University of Tokyo), National Institute for Environmental Studies, and Frontier Research Center for Global Change, available at : http://ccsr.aori.u-tokyo.ac.jp/~hasumi/miroc_description.pdf, 2004

Kanakidou, M., Seinfeld, J. H., Pandis, S. N., Barnes, I., Dentener, F. J., Facchini, M. C., Van Dingenen, R., Ervens, B., Nenes, A., Nielsen, C. J., Swietlicki, E., Putaud, J. P., Balkanski, Y., Fuzzi, S., Horth, J., Moortgat, G. K., Winterhalter, R., Myhre, C. E. L., Tsigaridis, K., Vignati, E., Stephanou, E. G., and Wilson, J. : Organic aerosol and global climate modelling: a review. *Atmos. Chem. Phys.*, 5(4), 1053-1123, <https://doi.org/10.5194/acp-5-1053-2005>

Kanaya, Y., Irie, H., Takashima, H., Iwabuchi, H., Akimoto, H., Sudo, K., Gu, M., Chong, J., Kim, Y. J., Lee, H., Li, A., Si, F., Xu, J., Xie, P.-H., Liu, W.-Q., Dzhola, A., Postolyakov, O., Ivanov, V., Grechko, E., Terpugova, S., and Panchenko, M.: Long-term MAX-DOAS network observations of NO₂ in Russia and Asia (MADRAS) during the period 2007–2012: instrumentation, elucidation of

climatology, and comparisons with OMI satellite observations and global model simulations. *Atmos. Chem. Phys.*, 14(15), 7909-7927, <https://doi.org/10.5194/acp-14-7909-2014>, 2014

Kannari, A., Tonooka, Y., Baba, T., & Murano, K. : Development of multiple-species 1km× 1km resolution hourly basis emissions inventory for Japan. *Atmos. Environ.*, 41(16), 3428-3439. doi:<https://doi.org/10.1016/j.atmosenv.2006.12.015>, 2007

Khodmanee, S., & Amnuaylojaroen, T., Impact of Biomass Burning on Ozone, Carbon Monoxide, and Nitrogen Dioxide in Northern Thailand. *Front. Environ. Sci.*, 9, 27. doi:<https://doi.org/10.3389/fenvs.2021.641877>, 2021

Kreher, K., Van Roozendaal, M., Hendrick, F., Apituley, A., Dimitropoulou, E., Frieß, U., Richter, A., Wagner, T., Lampel, J., Abuhassan, N., Ang, L., Anguas, M., Bais, A., Benavent, N., Bösch, T., Bogner, K., Borovski, A., Bruchkouski, I., Cede, A., Chan, K. L., Donner, S., Drosoglou, T., Fayt, C., Finkenzeller, H., Garcia-Nieto, D., Gielen, C., Gómez-Martín, L., Hao, N., Henzing, B., Herman, J. R., Hermans, C., Hoque, S., Irie, H., Jin, J., Johnston, P., Khayyam Butt, J., Khokhar, F., Koenig, T. K., Kuhn, J., Kumar, V., Liu, C., Ma, J., Merlaud, A., Mishra, A. K., Müller, M., Navarro-Comas, M., Ostendorf, M., Pazmino, A., Peters, E., Pinardi, G., Pinharanda, M., Pithers, A., Platt, U., Postolyakov, O., Prados-Roman, C., Puertedura, O., Querel, R., Saiz-Lopez, A., Schönhardt, A., Schreier, S. F., Seyler, A., Sinha, V., Spinei, E., Strong, K., Tack, F., Tian, X., Tiefengraber, M., Tirpitz, J.-L., van Gent, J., Volkamer, R., Vrekoussis, M., Wang, S., Wang, Z., Wenig, M., Wittrock, F., Xie, P. H., Xu, J., Yela, M., Zhang, C., and Zhao, X.: Intercomparison of NO₂, O₄, O₃ and HCHO slant column measurements by MAX-DOAS and zenith-sky UV–visible spectrometers during CINDI-2. *Atmos. Meas. Tech.*, 13(5), 2169-2208, <https://doi.org/10.5194/amt-13-2169-2020>, 2020

Kumar, V., Beirle, S., Dörner, S., Mishra, A. K., Donner, S., Wang, Y., Sinha, V., and Wagner, T. (2020). Long-term MAX-DOAS measurements of NO₂, HCHO, and aerosols and evaluation of corresponding satellite data products over Mohali in the Indo-Gangetic Plain. *Atmos. Chem. Phys.*, 20(22), 14183-14235. doi:10.5194/acp-20-14183-2020

1468 Kumar, V., & Sinha, V. (2021), Season-wise analyses of VOCs, hydroxyl radicals and ozone formation chemistry
 1469 over north-west India reveal isoprene and acetaldehyde as the most potent ozone precursors throughout the
 1470 year. *Chemosphere*, 283, 131184. doi:<https://doi.org/10.1016/j.chemosphere.2021.131184>
 1471
 1472
 1473 Kurucz, R. L., Furenlid, I., Brault, J., and Testerman, L. : Solar Flux Atlas from 296 to 1300 nm.
 1474 *Natl. Sol. Obs., Sunspot, New Mexico*, 240, 1984
 1475
 1476 Lee, M., Heikes, B. G., Jacob, D. J., Sachse, G., and Anderson, B. : Hydrogen peroxide, organic hydroperoxide,
 1477 and formaldehyde as primary pollutants from biomass burning, *J. Geophys. Res.*, 102(D1), 1301-1309,
 1478 <https://doi.org/10.1029/96JD01709>, 1997
 1479
 1480
 1481
 1482
 1483
 1484
 1485
 1486
 1487
 1488 Lin, S.-J., & Rood, R. B. : Multidimensional flux-form semi-Lagrangian transport schemes. *Mon. Weather Rev.*,
 1489 124(9), 2046-2070, [https://doi.org/10.1175/1520-0493\(1996\)124<2046:MFFSLT>2.0.CO;2](https://doi.org/10.1175/1520-0493(1996)124<2046:MFFSLT>2.0.CO;2), 1996
 1490
 1491 Ma, J., Beirle, S., Jin, J., Shaiganfar, R., Yan, P., and Wagner, T. : Tropospheric NO₂ vertical column densities
 1492 over Beijing: results of the first three years of ground-based MAX-DOAS measurements (2008–2011) and
 1493 satellite validation, *Atmos. Chem. Phys.*, 13(3), 1547-1567, <https://doi.org/10.5194/acp-13-1547-2013>,
 1494 2013
 1495
 1496
 1497 Mallik, C., & Lal, S. : Seasonal characteristics of SO₂, NO₂, and CO emissions in and around the Indo-Gangetic
 1498 Plain, *Environ Monit Assess*, 186(2), 1295-1310, <https://doi.org/10.1007/s10661-013-3458-y>, 2015

1499

1500 Martin, R. V., Fiore, A. M., and Van Donkelaar, A. : Space-based diagnosis of surface ozone sensitivity to
1501 anthropogenic emissions, *Geophys. Res. Lett.*, 31(6), <https://doi.org/10.1029/2004GL019416>, 2004

1502

1503

1504 Mahajan, A. S., De Smedt, I., Biswas, M. S., Ghude, S., Fadnavis, S., Roy, C., and van Roozendaal, M. : Inter-
1505 annual variations in satellite observations of nitrogen dioxide and formaldehyde over India. *Atmos.*
1506 *Environ.*, 116, 194-201, <https://doi.org/10.1016/j.atmosenv.2015.06.004>, 2015

1507

1508

1509

1510

1511

1512

1513

1514 Meller, R., and G. K. Moortgat. : Temperature dependence of the absorption cross sections of formaldehyde
1515 between 223 and 323 K in the wavelength range 225–375 nm, *J. Geophys. Res.*, 105(D6), 7089-7101,
1516 doi:10.1029/1999JD901074, 2000

1517

1518

1519

1520 Mellor, G. L., & Yamada, T. : A hierarchy of turbulence closure models for planetary boundary layers. *J. Atmos.*
1521 *Sci.*, 31(7), 1791-1806, [https://doi.org/10.1175/1520-0469\(1974\)031<1791:AHOTCM>2.0.CO;2](https://doi.org/10.1175/1520-0469(1974)031<1791:AHOTCM>2.0.CO;2), 1974

1522

1523

1524 Mishra, A. K., and Sinha, V. : Emission drivers and variability of ambient isoprene, formaldehyde and
1525 acetaldehyde in north-west India during monsoon season, *Environ. Pollut.*, 267, 115538,
1526 <https://doi.org/10.1016/j.envpol.2020.115538>, 2020

1527

1528 Miyazaki, K., Bowman, K., Sekiya, T., Eskes, H., Boersma, F., Worden, H., Livesey, N., Payne, V.H., Sudo, K.,
1529 Kanaya, Y., Takigawa, M., and Ogochi, K. (2020). Updated tropospheric chemistry reanalysis and

emission estimates, TCR-2, for 2005–2018. *Earth Syst. Sci. Data*, 12(3), 2223-2259. doi:10.5194/essd-12-2223-2020

Miyazaki, K., Eskes, H., Sudo, K., Boersma, K. F., Bowman, K., and Kanaya, Y. : Decadal changes in global surface NO_x emissions from multi-constituent satellite data assimilation. *Atmos. Chem. Phys.*, 17(2), 807-837, <https://doi.org/10.5194/acp-17-807-2017>, 2017

Morino, Y., Ohara, T., Yokouchi, Y., & Ooki, A. : Comprehensive source apportionment of volatile organic compounds using observational data, two receptor models, and an emission inventory in Tokyo metropolitan area. *J. Geophys. Res.*, 116(D2),doi:<https://doi.org/10.1029/2010JD014762>, 2011

Nair, V. S., Moorthy, K. K., Alappattu, D. P., Kunhikrishnan, P.K., George, S., Nair, P. R., Babu, S.S., Abish, A., Satheesh, S.K., Tripathi, S. N., Niranjana, K., Madhavan, B.L., Srikant, V., Dutt, C.B.S., Badarinath, K>V>S., & Reddy, R.R.: Wintertime aerosol characteristics over the Indo-Gangetic Plain (IGP): Impacts of local boundary layer processes and long-range transport. *J. Geophys. Res.*, 112(D13). doi:<https://doi.org/10.1029/2006JD008099>, 2007

Ohara, T., Akimoto, H., Kurokawa, J., Horii, N., Yamaji, K., Yan, X., & Hayasaka, T. : An Asian emission inventory of anthropogenic emission sources for the period 1980–2020. *Atmos. Chem. Phys.*, 7(16), 4419-4444. doi:<https://doi.org/10.5194/acp-7-4419-2007>, 2007

Platt, U. : Differential optical absorption spectroscopy (DOAS), in *Chemical Analysis Series*, edited, pp. 27-84, Wiley & Sons. Inc., 1994

Platt, U., and Stutz, J. : *Differential Optical Absorption Spectroscopy*, Springer, 2008

Price, C., & Rind, D. : A simple lightning parameterization for calculating global lightning distributions. *J. Geophys. Res.*, 97(D9), 9919-9933, <https://doi.org/10.1029/92JD00719>, 1992

Rodgers, C. D. : *Inverse methods for atmospheric sounding: theory and practice*, World scientific Singapore, 2008

1566 Roscoe, H. K., Van Roozendaal, M., Fayt, C., du Piesanie, A., Abuhassan, N., Adams, C., Akrami, M., Cede, A.,
 1567 Chong, J., Clémer, K., Friess, U., Gil Ojeda, M., Goutail, F., Graves, R., Griesfeller, A., Grossmann, K.,
 1568 Hemerijckx, G., Hendrick, F., Herman, J., Hermans, C., Irie, H., Johnston, P. V., Kanaya, Y., Kreher, K.,
 1569 Leigh, R., Merlaud, A., Mount, G. H., Navarro, M., Oetjen, H., Pazmino, A., Perez-Camacho, M., Peters,
 1570 E., Pinardi, G., Puentedura, O., Richter, A., Schönhardt, A., Shaiganfar, R., Spinei, E., Strong, K.,
 1571 Takashima, H., Vlemmix, T., Vrekoussis, M., Wagner, T., Wittrock, F., Yela, M., Yilmaz, S., Boersma,
 1572 F., Hains, J., Kroon, M., Piter, A., and Kim, Y. J. : Intercomparison of slant column measurements of NO₂
 1573 and O₄ by MAX-DOAS and zenith-sky UV and visible spectrometers. *Atmos. Meas. Tech.*, 3(6), 1629-
 1574 1646, <https://doi.org/10.5194/amt-3-1629-2010>, 2010
 1575
 1576
 1577 Ryan, R. G., Rhodes, S., Tully, M., & Schofield, R. : Surface ozone exceedances in Melbourne, Australia are
 1578 shown to be under NO_x control, as demonstrated using formaldehyde: NO₂ and glyoxal: formaldehyde
 1579 ratios, *Sci. Total Environ.*, 749, 141460, <https://doi.org/10.1016/j.scitotenv.2020.141460>, 2020
 1580
 1581 Sadavarte, P., & Venkataraman, C. : Trends in multi-pollutant emissions from a technology-linked inventory for
 1582 India: I. Industry and transport sectors. *Atmos. Environ.*, 99, 353-364.
 1583 doi:<https://doi.org/10.1016/j.atmosenv.2014.09.081>, 2014
 1584
 1585 Sarmah, S., Singha, M., Wang, J., Dong, J., Burman, P. K. D., Goswami, S., Ge. Y., Ilyas, S., & Niu, S. :
 1586 Mismatches between vegetation greening and primary productivity trends in South Asia—A satellite
 1587 evidence. *Int. J. Appl. Earth Obs.*, 104, 102561. doi:<https://doi.org/10.1016/j.jag.2021.102561>, 2021
 1588
 1589
 1590 Schindlbacher, A., Zechmeister-Boltenstern, S., & Butterbach-Bahl, K. : Effects of soil moisture and temperature
 1591 on NO, NO₂, and N₂O emissions from European forest soils. *J. Geophys. Res.*, 109(D17),
 1592 <https://doi.org/10.1029/2004JD004590>, 2004
 1593
 1594 Schroeder, J. R., Crawford, J. H., Fried, A., Walega, J., Weinheimer, A., Wisthaler, A., Muller, M., Mikovinu, T.,
 1595 Chen, G., Shook, M. : New insights into the column CH₂O/NO₂ ratio as an indicator of near-surface ozone
 1596 sensitivity. *J. Geophys. Res.*, 122(16), 8885-8907. doi: <https://doi.org/10.1002/2017JD026781>, 2017
 1597
 1598 Sharma, S., Goel, A., Gupta, D., Kumar, A., Mishra, A., Kundu, S., Chatani, S., and Klimont, Z. : Emission
 1599 inventory of non-methane volatile organic compounds from anthropogenic sources in India. *Atmos.*
 1600 *Environ.*, 102, 209-219. doi:<https://doi.org/10.1016/j.atmosenv.2014.11.070>, 2015

1601
 1602
 1603
 1604 Seco, R., Penuelas, J., and Filella, I. : Short-chain oxygenated VOCs: Emission and uptake by plants and
 1605 atmospheric sources, sinks, and concentrations, *Atmos. Environ.*, 41(12), 2477-2499,
 1606 <https://doi.org/10.1016/j.atmosenv.2006.11.029>, 2007
 1607
 1608
 1609
 1610 Sekiya, T., & Sudo, K. : Roles of transport and chemistry processes in global ozone change on interannual and
 1611 multidecadal time scales. *J. Geophys. Res.*, 119(8), 4903-4921.
 1612 doi:<https://doi.org/10.1002/2013JD020838>, 2014
 1613
 1614 Sekiya, T., Miyazaki, K., Ogochi, K., Sudo, K., & Takigawa, M. : Global high-resolution simulations of
 1615 tropospheric nitrogen dioxide using CHASER V4.0. *Geosci. Model Dev.*, 11(3), 959-988.
 1616 <http://doi.org/10.5194/gmd-11-959-2018>, 2018
 1617
 1618 Seinfeld, J. H., & Pandis, S. N. : Atmospheric chemistry and physics: from air pollution to climate change: John
 1619 Wiley & Sons, New York, 1998
 1620
 1621 Sindelarova, K., Markova, J., Simpson, D., Huszar, P., Karlicky, J., Darras, S., & Granier, C. : High-resolution
 1622 biogenic global emission inventory for the time period 2000–2019 for air quality modelling. *Earth Syst.*
 1623 *Sci. Data*, 14(1), 251-270. doi:<https://doi.org/10.5194/essd-14-251-2022>, 2022
 1624
 1625 Singh, H., Salas, L., Chatfield, R., Czech, E., Fried, A., Walega, J., Evans, M.J., Field, B.D., Jacob, D.J., Blake,
 1626 D., Heikes, B., Talbott, R., Sachse, G., Crawford, J.H., Avery, M.A., Sandholm, S., and Fuelberg, H. :
 1627 Analysis of the atmospheric distribution, sources, and sinks of oxygenated volatile organic chemicals based
 1628 on measurements over the Pacific during TRACE-P, *J. Geophys. Res.*, 109(D15),
 1629 <https://doi.org/10.1029/2003JD003883>, 2004
 1630

1631 Sinreich, R., Frieß, U., Wagner, T., and Platt, U. : Multi axis differential optical absorption spectroscopy (MAX-
 1632 DOAS) of gas and aerosol distributions, Faraday discuss., 130, 153-164,
 1633 <https://doi.org/10.1039/B419274P>, 2005
 1634
 1635

1636 Solomon, S., Portmann, R., Sanders, R., Daniel, J., Madsen, W., Bartram, B., and Dutton, E. : On the role of
 1637 nitrogen dioxide in the absorption of solar radiation, J. Geophys. Res., 104(D10), 12047-12058,
 1638 <https://doi.org/10.1029/1999JD900035>, 1999
 1639
 1640

1641 Souri, A. H., Nowlan, C. R., Wolfe, G. M., Lamsal, L. N., Miller, C. E. C., Abad, G. G., Janz, S., Fried, A., Blake,
 1642 D. R., Weinheimer, A. J. , Diskin, G.S., Liu, X., and Chance, K. : Revisiting the effectiveness of
 1643 HCHO/NO₂ ratios for inferring ozone sensitivity to its precursors using high resolution airborne remote
 1644 sensing observations in a high ozone episode during the KORUS-AQ campaign. Atmos. Environ., 224,
 1645 117341, <https://doi.org/10.1016/j.atmosenv.2020.117341>, 2020
 1646
 1647

1648 Sudo, K., & Akimoto, H. (2007). Global source attribution of tropospheric ozone: Long-range transport from
 1649 various source regions. J. Geophys. Res., 112(D12), <https://doi.org/10.1029/2006JD007992>, 2007
 1650

1651 Sudo, K., Takahashi, M., Kurokawa, J., & Akimoto, H. : CHASER: A global chemical model of the troposphere
 1652 1. Model description. J. Geophys. Res., 107, 4339, <https://doi.org/10.1029/2001JD001113>, 2002
 1653

1654 Surl, L., Palmer, P. I., & González Abad, G. : Which processes drive observed variations of HCHO columns over
 1655 India? Atmos. Chem. Phys., 18(7), 4549-4566 ,<https://doi.org/10.5194/acp-18-4549-2018>, 2018
 1656
 1657

1658 Takemura, T., Nozawa, T., Emori, S., Nakajima, T. Y., & Nakajima, T. : Simulation of climate response to aerosol
 1659 direct and indirect effects with aerosol transport-radiation model. J. Geophys. Res., 110(D2),
 1660 <https://doi.org/10.1029/2004JD005029>, 2005
 1661

1662 Takemura, T., Egashira, M., Matsuzawa, K., Ichijo, H., O'ishi, R., & Abe-Ouchi, A. : A simulation of the global
 1663 distribution and radiative forcing of soil dust aerosols at the Last Glacial Maximum. *Atmos. Chem. Phys.*,
 1664 9(9), 3061-3073, <https://doi.org/10.5194/acp-9-3061-2009>, 2009
 1665
 1666 Tonnesen, G. S., & Dennis, R. L. (2000). Analysis of radical propagation efficiency to assess ozone sensitivity to
 1667 hydrocarbons and NO_x: 1. Local indicators of instantaneous odd oxygen production sensitivity. *J. Geophys.*
 1668 *Res.*, 105(D7), 9213-9225. doi:<https://doi.org/10.1029/1999JD900371>
 1669
 1670
 1671 Vandaele, A., C. Hermans, P. Simon, M. Van Roozendael, J. Guilmot, M. Carleer, and R. Colin.: Fourier
 1672 transform measurement of NO₂ absorption cross-section section in the visible range at room temperature,
 1673 *J. Atmos. Chem.*, 25(3), 289-305, doi:10.1007/BF00053797, 2009
 1674
 1675
 1676 Vandaele, A. C., C. Fayt, F. Hendrick, C. Hermans, F. Humbled, M. V. Roozendael, M. Gil, M. Navarro, O.
 1677 Puertedura, M. Yela, G. Braathen, K. Stebel, K. Tornkvist, P. Jhonston, K. Kreher, F. Goutail, F. Mieville,
 1678 J.P. Pommereau, S. Khaikine, A. Richter, H. Oetjen, F. Wittrock, S. Bugarski, U. Friess, K. Pfeilsticker,
 1679 R. Sinreich, T. Wagner, G. Corlett, and R. Leigh), An intercomparison campaign of ground-based UV-
 1680 visible measurements of NO₂, BrO, and OClO slant columns Methods of analysis and results for NO₂, *J.*
 1681 *Geophys Res*, 110(D8),2005
 1682
 1683
 1684 Vigouroux, C., Hendrick, F., Stavrakou, T., Dils, B., De Smedt, I., Hermans, C., Merlaud, A., Scolas, F., Senten,
 1685 C., Vanhaelewyn, G., Fally, S., Carleer, M., Metzger, J.-M., Müller, J.-F., Van Roozendael, M., and De
 1686 Mazière, M.: Ground-based FTIR and MAX-DOAS observations of formaldehyde at Réunion Island and
 1687 comparisons with satellite and model data, *Atmos. Chem. Phys.*, 9(24), 9523-9544,
 1688 <https://doi.org/10.5194/acp-9-9523-2009>, 2009
 1689
 1690
 1691
 1692

1693 Wagner, T., Dix, B. v., Friedeburg, C. v., Frieß, U., Sanghavi, S., Sinreich, R., & Platt, U. : MAX-DOAS O4
1694 measurements: A new technique to derive information on atmospheric aerosols—Principles and
1695 information content. *J. Geophys. Res.*, 109(D22). doi: <https://doi.org/10.1029/2004JD004904>, 2004
1696

1697 Wagner, T., Burrows, J., Deutschmann, T., Dix, B., Friedeburg, C. v., Frieß, U., Iwabuchi, H. , Hendrick, F., Heue,
1698 K.-P., Irie, H., Iwabuchi, H., Kanaya, Y., Keller, J., McLinden, C. A., Oetjen, H., Palazzi, E., Petritoli, A.,
1699 Platt, U., Postlyakov, O., Pukite, J., Richter, A., van Roozendaal, M., Rozanov, A., Rozanov, V., Sinreich,
1700 R., Sanghavi, S., and Wittrock, F. : Comparison of box-air-mass-factors and radiances for Multiple-Axis
1701 Differential Optical Absorption Spectroscopy (MAX-DOAS) geometries calculated from different
1702 UV/visible radiative transfer models. *Atmos. Chem. Phys.*, 7(7), 1809-1833.
1703 doi:<https://doi.org/10.5194/acp-7-1809-2007>, 2007
1704

1705

1706 Wang, T., Hendrick, F., Wang, P., Tang, G., Clémer, K., Yu, H., Fayt, C., Hermans, C., Gielen, C., Müller, J.-F.,
1707 Pinardi, G., Theys, N., Brenot, H., and Van Roozendaal, M. : Evaluation of tropospheric SO₂ retrieved
1708 from MAX-DOAS measurements in Xianghe, China. *Atmos. Chem. Phys.*, 14(20), 11149-11164,
1709 <https://doi.org/10.5194/acp-14-11149-2014>, 2014
1710

1711

1712

1713

1714 Wesely, M. : Parameterization of surface resistances to gaseous dry deposition in regional-scale numerical models.
1715 *Atmos. Environ.*, 41, 52-63. <https://doi.org/10.1016/j.atmosenv.2007.10.058>, 1989
1716

1717 Williams, J. E., Boersma, K. F., Sager, P. L., & Verstraeten, W. W.. The high-resolution version of TM5-MP for
1718 optimized satellite retrievals: description and validation. *Geosci. Model Dev.*, 10(2), 721-750.
1719 doi:<https://doi.org/10.5194/gmd-10-721-2017>, 2017
1720

1721

1722 Wittrock, F., Oetjen, H., Richter, A., Fietkau, S., Medeke, T., Rozanov, A., and Burrows, J. : MAX-DOAS
1723 measurements of atmospheric trace gases in Ny-Ålesund-Radiative transfer studies and their application,
1724 *Atmos. Chem. Phys.*, 4(4), 955-966, <https://doi.org/10.5194/acp-4-955-2004>, 2004

1725
1726
1727
1728
1729
1730
1731
1732
1733

Woo, J-H., Kim, Y. , Kim, H-K., Choi, K-C., Eum, J-H., Lee, J-B., Lim, J-H., Kim,J., and Seong, M. : Development of the CREATE inventory in support of integrated climate and air quality modeling for Asia. Sustainability, 12(19), 7930. doi:<https://doi.org/10.3390/su12197930>, 2020